

REPORT DOCUMENTATION PAGE

1. REPORT SECURITY CLASSIFICATION Unclassified		10. RESTRICTIVE MARKINGS	
2. SECURITY CLASSIFICATION AUTHORITY Unclassified		3. DISTRIBUTION/AVAILABILITY OF REPORT Approved for public release, distribution is unlimited	
4. DECLASSIFICATION/DOWNGRADING SCHEDULE			
5. PERFORMING ORGANIZATION REPORT NUMBER(S) F49620-92-J-0518		6. MONITORING ORG A AFOSR-TR-96	
7. NAME OF PERFORMING ORGANIZATION Georgia Institute of Technology		8. OFFICE SYMBOL (If applicable) AFOSR/NA	
9. ADDRESS (City, State and ZIP Code) School of Mechanical Engineering Atlanta, GA 30332-0405		10. ADDRESS (City, State and ZIP Code) 110 Duncan Avenue, Suite B115 Bolling AFB DC 20332-0001	
11. NAME OF FUNDING/SPONSORING ORGANIZATION AFOSR/NA		12. OFFICE SYMBOL (If applicable) NA	
13. ADDRESS (City, State and ZIP Code) 110 Duncan Avenue, Suite B115 Bolling AFB DC 20332-0001		14. PROCUREMENT INSTRUMENT IDENTIFICATION NUMBER F49620-92-J-0518	
15. TITLE (Include Security Classification) Novel Diagnostic Techniques and Actuator Technology for Turbulent Shear Flows		16. SOURCE OF FUNDING NOS. PROGRAM ELEMENT NO. PE-61102F PROJECT NO. PR-2308 TASK NO. SA-BS WORK UNIT NO. G-F49620-92-J-0518	
17. PERSONAL AUTHORISI Ari Glezer			
18. TYPE OF REPORT Final Technical Report		19. TIME COVERED FROM 18 Sep 92 TO 26 Feb 96	
20. DATE OF REPORT (Yr., Mo., Day) 1996, April 30		21. PAGE COUNT 174	
22. SUPPLEMENTARY NOTATION			
23. COSATI CODES		24. SUBJECT TERMS (Continue on reverse if necessary and identify by block numbers) fluidic actuators, synthetic jet, thrust vectoring, direct small scale mixing, vorticity, ultrasound scattering	
25. ABSTRACT (Continue on reverse if necessary and identify by block numbers) The research program is comprised of three major thrust areas: i) Novel fluidic actuator technology: A new approach to the manipulation and control of shear flows using fluidic technology based on jet actuators that are synthesized from the working fluid in the flow system in which they are embedded has been developed. Synthetic jets can effect significant global modifications on embedding flows on scales that are one to two orders of magnitude larger than the characteristic length scale of the jets themselves. This technology was applied to the vectoring of a high aspect ratio rectangular jets either towards or away from the actuator. Strong instabilities of the jet column are excited when the control jets are amplitude-modulated resulting in substantial increase in small scale motions and entrainment into the primary jet and thus increased levels of mixedness. ii) Mixing enhancement by direct small-scale manipulation: The concept of direct excitation of the small scales that bypasses the conventional energy cascade is demonstrated by forcing a shear layer segment near the exit plane of an air jet emanating from a square conduit near the passage frequency of the Kolmogorov scale. When the flow is forced, the dissipation increases by more than an order of magnitude relative to the unforced flow and the rate of decay of turbulent kinetic energy is increased, along with energy transfer from the large scales to the small scales. Excitation of a few discrete wavenumbers within the dissipation range of the jet shear layer, using amplitude modulation of the excitation waveform, leads to the emergence of discrete wavenumbers one to two orders of magnitude smaller. iii) Vorticity measurements using ultrasound scattering: Ultrasound scattering is used as a non-intrusive spectral probe of vorticity in a swirling air jet by exploiting the linear relationship between the Fourier component of the scattered acoustic pressure from an ultrasonic plane wave that is propagating through the flow and the Fourier transform of the vorticity component. The scattered ultrasound in the radial direction is measured at a number of streamwise and azimuthal stations. Fourier components of the uniform vorticity distribution are directly measured by varying the scattering angle and are in good agreement with theoretical predictions.			
26. DISTRIBUTION/AVAILABILITY OF ABSTRACT <input checked="" type="checkbox"/> SAME AS RPT <input type="checkbox"/> DTIC USERS <input type="checkbox"/>		27. ABSTRACT SECURITY CLASSIFICATION Unclassified	
28. NAME OF RESPONSIBLE INDIVIDUAL DR. JAMES McMICHAEL		29. TELEPHONE NUMBER (Include Area Code) 202-767-4935	
30. FORM 1473, 83 APR		31. OFFICE SYMBOL NA	
32. EDITION OF 1 JAN 73 IS OBSOLETE.			

**NOVEL DIAGNOSTIC TECHNIQUES AND ACTUATOR
TECHNOLOGY FOR TURBULENT SHEAR FLOWS**

AFOSR GRANT F49620-92-J-0518

**FINAL TECHNICAL REPORT
September 1, 1992 - February 29, 1996**

Submitted to

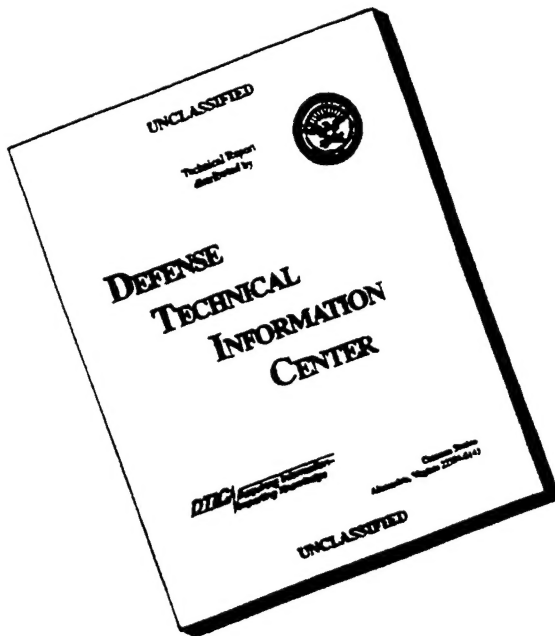
Dr. James M. McMichael
Air Force Office of Scientific Research
Bolling Air Force Base, Building 410
Washington, D.C. 20332

submitted by

Dr. Ari Glezer
Woodruff School of Mechanical Engineering
Georgia Institute of Technology
Atlanta, GA 30332-0405

19961017 140

DISCLAIMER NOTICE



THIS DOCUMENT IS BEST
QUALITY AVAILABLE. THE
COPY FURNISHED TO DTIC
CONTAINED A SIGNIFICANT
NUMBER OF PAGES WHICH DO
NOT REPRODUCE LEGIBLY.

I. SUMMARY OF RESEARCH PROGRAM

The research program funded under this grant has had three major thrust areas:

I.1. Novel fluidic actuator technology and its application to thrust vectoring.

A new approach to the manipulation and control of shear flows using novel fluidic technology based on synthetic jets has been developed. These jets have the unique property of being *zero-mass-flux* in nature; i.e., they are synthesized from the working fluid in the flow system in which they are embedded. Although there is no net mass injection into the overall system, the jets allow momentum transfer into the embedding flow. The interaction of synthetic jets and an embedding flow near the flow boundary leads to the formation of closed recirculation regions and thus an *apparent* modification of the flow boundary. *These features enable synthetic jets to effect significant global modifications in embedding flows on scales that are one to two orders of magnitude larger than the characteristic length scale of the jets themselves.*

This actuation technology was applied to the vectoring of a high aspect ratio rectangular jet (7 m/sec, 7.62 x 1.27 cm) using co-flowing, millimeter-scale synthetic control jets. The control jets have an orifice width of 0.5 mm span the entire width of the primary jet nozzle and are placed along each of the long sides and near the exit plane of the primary jet. The ratio of the momentum flux in the cross-stream plane between each control jet and the primary jet is 1:35. The present experiments have demonstrated that each control jet can vector the primary jet at angles exceeding $\pm 30^\circ$ without an appreciable increase in the cross-stream spreading of the primary jet. A unique feature of the synthetic jet actuators is that *vectoring can be directed either towards or away from the actuator*. Thus, when the two control are operated in concert, the primary jet is vectored at angles exceeding $\pm 80^\circ$. Strong instabilities of the jet column are excited when the control jets are amplitude-modulated resulting in substantial increase in small scale motions and entrainment into the primary jet and thus increased levels of mixedness.

I.2. Mixing enhancement by *direct* small-scale manipulation

Control of small-scale mixing in free shear flows by manipulation of global two- and three-dimensional instability modes and the ensuing vortical structures, depends on the classical cascading mechanism to transfer control influence to the scales at which molecular mixing occurs. Thus, mixing at the smallest scales in fully turbulent flows is *indirect* and only *weakly coupled* to the control input. The concept of direct excitation of the small

scales that bypasses the conventional energy cascade is demonstrated by forcing a shear layer segment near the exit plane of an air jet emanating from a square conduit (3.81 x 3.81 cm, 6.5 m/sec) near the passage frequency of the Kolmogorov scale. Distributions of the streamwise velocity component are measured upstream of the interaction of the four shear layer segments using hot wire anemometry. It is found that when the flow is forced, the dissipation increases by more than an order of magnitude relative to the unforced flow. Moreover, the rate of decay of turbulent kinetic energy is increased, along with energy transfer from the large scales to the small scales. Excitation of a number of discrete wavenumbers within the dissipation range of the jet shear layer, using amplitude modulation of the excitation waveform, leads to the emergence of discrete wavenumbers one to two orders of magnitude smaller.

and

I.3. Novel technique for nonintrusive vorticity measurements using ultrasound scattering.

That ultrasound scattering can be used as a non-intrusive spectral probe of vorticity and potentially as a tool for direct measurements of vorticity distributions is demonstrated in a swirling air jet by exploiting the linear relationship between the Fourier component of the scattered acoustic pressure from an ultrasonic plane wave that is propagating through the flow and the Fourier transform of the vorticity component. The measured vorticity component is normal to the plane defined by the wave vectors of the incident and scattered acoustic waves. The swirling air jet emanates from a 2.54 cm diameter nozzle and the swirl (swirl numbers up to 0.4 are realized) is generated upstream of the jet nozzle by a rotating paddle. A nominally plane ultrasonic wave field is generated normal to the jet axis by a transmitter having a 16 cm square aperture. The scattered ultrasound in the radial direction is measured at a number of streamwise and azimuthal stations. In accord with the theory, the normalized amplitude of the scattered acoustic wave is a linear function of the angular velocity of the swirl generator, and is independent of the intensity of the incident wave field. Fourier components of the uniform vorticity distribution are directly measured by varying the scattering angle and are in good agreement with theoretical predictions.

II. FLUIDIC ACTUATOR TECHNOLOGY BASED ON SYNTHETIC JETS

II.1. Technical Background

Fluidic actuators employing control jets to affect a primary jet of the same fluid within an enclosed cavity have been studied since the late 1950's. These actuators perform a variety of "analog" (e.g., proportional fluidic amplifier) and "digital" (e.g., flip-flop) throttling and control functions in flow systems without moving mechanical parts (Joyce, 1983). In the "analog" actuator, the volume flow rate fraction of two opposite control jets leads to a proportional change in the volume flow rate of the primary stream out of two corresponding output ports. The "digital" actuator is a bistable flow device in which the control jets and Coanda effect are used to direct the primary stream into one of two output ports. Although most of the fluidic technology has been restricted to enclosed cavities, some of these devices have also been used in free shear flows. Viets (1975) induced spontaneous oscillations in a free rectangular jet by exploiting the concept of a flip-flop actuator. More recently, Raman and Cornelius (1995) used two such jets to impose time harmonic oscillations in a larger jet by direct impingement. The control jets were placed on opposite sides of the primary jet and could be operated in phase or out of phase with each other.

We have recently developed a radically new approach to the manipulation and control of shear flows using novel fluidic technology based on synthetic jets. These jets have the unique property of being *zero-mass-flux* in nature; i.e., they are synthesized from the working fluid in the flow system in which they are embedded. Although there is no net mass injection into the overall system, the jets allow momentum transfer into the embedding flow. The interaction of synthetic jets and an embedding flow near the flow boundary leads to the formation of closed recirculation regions and thus an *apparent* modification of the flow boundary. *These features enable synthetic jets to effect significant global modifications in embedding flows on scales that are one to two orders of magnitude larger than the characteristic length scale of the jets themselves.* Furthermore, while conventional excitation schemes have been limited to frequency bands tailored to the linear receptivity mechanisms of a given flow, fluidic actuation allows for exploitation of nonlinear mechanisms for amplification of disturbances in a very broad frequency band. These capabilities have been demonstrated in a series of pilot investigations including thrust vectoring and modification of aerodynamic surfaces.

In current implementation of these devices, nominally round or plane turbulent jets are formed in air or water normal to an orifice in a flat plate. These jets operate without net mass injection across the actuator surface and are thus comprised entirely of entrained

surrounding fluid and are in effect synthesized by a train of vortices. Each vortex is formed at the edge of the orifice, and is driven by the motion of a diaphragm at the bottom of a sealed shallow cylindrical cavity under the orifice plate. The vortices, and thus the characteristic dimensions of the jets, scale with the characteristic dimension of the orifices. Because the motion of the diaphragm is extremely small and it can be driven at resonance (e.g., by a piezoelectric actuator), the electrical power input to the actuator is typically small (in recent experiments at Georgia Tech, a millimeter-scale synthetic jet actuator was used for thrust vectoring of primary jets that are at least two orders of magnitude larger where the power input of the actuator was several milliwatts).

That jet actuators are synthesized from the working fluid (gas or liquid) in the flow system in which they are embedded obviates the need for input piping and complex fluidic packaging, and makes them ideally suited for fabrication using micromachining techniques. Under support from AFOSR, we have designed, fabricated and tested microjet actuators having orifice diameters of the order of 150 μm (Coe, Allen, Trautman, and Glezer 1994). These actuators can be used to affect macro-scale events in a variety of applications: either *directly* from the concerted action of a large number of individually controllable microjets (for example, we have demonstrated that a micromachined array of 360 phased jets can generate sufficient thrust to move a suspended, packaged silicon die containing the microjets over an excursion distance of 30 cm); or *indirectly*, by amplifying their control input through a flow system that is used as a fluidic amplifier. This control scheme is particularly attractive for microjet actuators because the energy that is necessary to amplify the control input is extracted from the flow being influenced and, as a result, will allow the implementation of cascaded control. Specifically, that microjets be used in a scaling hierarchy to manipulate millimeter-scale jets which, in turn, will control larger jets.

In contrast to conventional jets, a unique feature of zero mass flux jets is that they are synthesized from the working fluid of the flow system in which they are deployed; thus transferring linear momentum to the flow system without net mass injection across the system boundary. Since these jets are comprised entirely of entrained ambient fluid, they are extremely effective in stirring and mixing of the working fluid in both closed and open flow systems, and in transporting heat from solid surfaces. Because zero mass flux jet actuators can be realized without input piping and complex fluidic packaging, they are ideally suited for deployment in large arrays in a number of applications where space constraints are an important issue.

Synthetic jets can be formed by streaming induced by the transmission of sound through fluid (often referred to as acoustic streaming) or by oscillating the boundaries of a quiescent medium. Such streaming motions have been the subject of a number of

investigations that demonstrated the establishment of steady rotational flow in air and in water by propagating and standing acoustic waves (e.g., Nyborg 1953, Westerveldt 1953, Ostrovskii and Papilova 1974, and Makarov *et al.* 1989), with fluid velocities of the order of 10-15 m/sec and 1-2 m/sec, respectively. Acoustic streaming is induced by the action of Reynolds stresses, but it is the dissipation of acoustic energy through the attenuation of transmitted sound or through the viscous effects at an oscillating solid boundary that leads to the fluid motion (Lighthill 1978). A number of investigations have also been concerned with streaming associated with oscillating solid boundaries, most notably time-harmonic oscillations of a cylinder normal to its axis (e.g., Stuart 1966, Davidson and Riley 1972, Riley and Wibrow 1995) leading to streaming velocities on the order of 1 cm/s in water at a nominal frequency of 45 Hz.

The formation of a jet without net mass flux was reported by Mednikov and Novitskii (1975), who used a low frequency (10-100 Hz) oscillating piston and bellows mechanism in a resonance cavity and measured average streaming velocities of up to 17 m/s. More recently, Lebedeva (1980) created a synthetic jet with velocities of up to 10 m/s, by transmitting high amplitude sound waves (150 dB) through an orifice placed at the end of a tube. Sheen *et al.* (1989) studied streaming in water due to an oscillating ultrasonic transducer that transmitted a longitudinal compression wave through a waveguide to the liquid.

More recently, James, Jacobs, and Glezer (1996) investigated the formation of and evolution of a synthetic round turbulent water jet produced normal to, and at the center of a submerged, resonantly driven actuator disk. The jet, formed without net mass injection and comprised entirely of radially entrained fluid, was produced only when a small cluster of cavitation bubbles appeared near the center of the actuator during each oscillation cycle of the actuator. Although no direct proof was given, it was conjectured that the time-periodic formation of these bubbles displace vorticity from the boundary layer of the actuator, and leads to the formation of vortex puffs that coalesce to form a synthesized turbulent jet. Single point measurements using LDV showed that the time averaged jet is similar to a conventional turbulent round jet in that the increase in both its width and in the inverse of its centerline velocity is a linear function of the distance from the actuator.

II.2. The Present Implementation

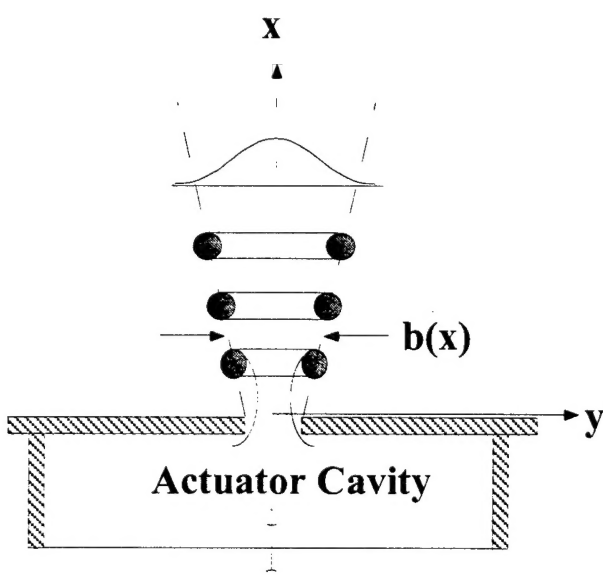
In the present implementation, nominally round (or plane) turbulent air (or liquid) jets are synthesized by a train of vortex rings (or two-dimensional vortex pairs). The vortices are formed at the edge of an actuator orifice by the motion of a small diaphragm that is driven by a piezoceramic disc and mounted at the bottom of a sealed shallow

cylindrical cavity as shown schematically in Figure II-1a. During the forward motion of the diaphragm, fluid is ejected from the cavity, the ensuing flow separates at the sharp edge of the orifice, forming a vortex sheet that rolls into a vortex ring that begins to move away from the orifice under its own self-induced velocity (Glezer & Coles 1990). When the diaphragm begins to move away from the orifice, the vortex is already sufficiently removed and is thus unaffected by the ambient fluid that is drawn into the cavity. Therefore, during each cycle the net mass flux out of the cavity is zero while the mass and hydrodynamic impulse of each vortex are non zero. The diaphragm is typically driven at resonance (e.g., by a piezoelectric actuator), and thus the electrical power input to the actuator is typically small (in recent experiments at Georgia Tech, a millimeter-scale synthetic jet actuator having a power input of several milliwatts, was used to vector a primary jets that was at least two orders of magnitude larger).

The jet is synthesized by the time-harmonic formation and subsequent interactions of these vortices, and, therefore, its characteristic dimensions scale with the characteristic dimension of the orifice. Thus, it is possible to synthesize jets over a broad range of characteristic cross flow length scales (two-dimensional and axisymmetric orifices have been fabricated in the millimeter and micrometer range). Furthermore, for a given amplitude of the diaphragm motion, the characteristic time scales associated with the period of the oscillations affect the total circulation of cores of individual vortices. The characteristic time scales also affect the response of the jet to changes in the amplitude of the motion of the diaphragm. Figure II-1b is a Schlieren image a two-dimensional synthetic air jet having a rectangular orifice that is 0.5 mm wide; it clearly shows a vortex pair formed near the orifice. The image also shows a streak of heated fluid entrained by the jet.

Cross-stream distributions of the streamwise velocity component were measured at a number of streamwise stations downstream from the orifice using hot wire anemometry. These data are plotted in Figure II-2a in the usual similarity coordinates and demonstrate that, at least within the streamwise domain of the present measurements, the jet is reasonably self-similar. The streamwise decay of the centerline velocity is shown in Figure II-2b. The streamwise decay rate of a conventional plane turbulent jet is also shown for reference. It is noted, however, that details of the flow field near the orifice and of the entrained flow far from the jet cannot be studied with any reasonable accuracy using conventional hot wire anemometry because hot wire sensors cannot resolve velocities below 0.5 m/sec or reversed flows.

Synthetic jet actuators have also been microfabricated using standard silicon micromachining techniques; they consist of an orifice situated atop an actuator cavity which

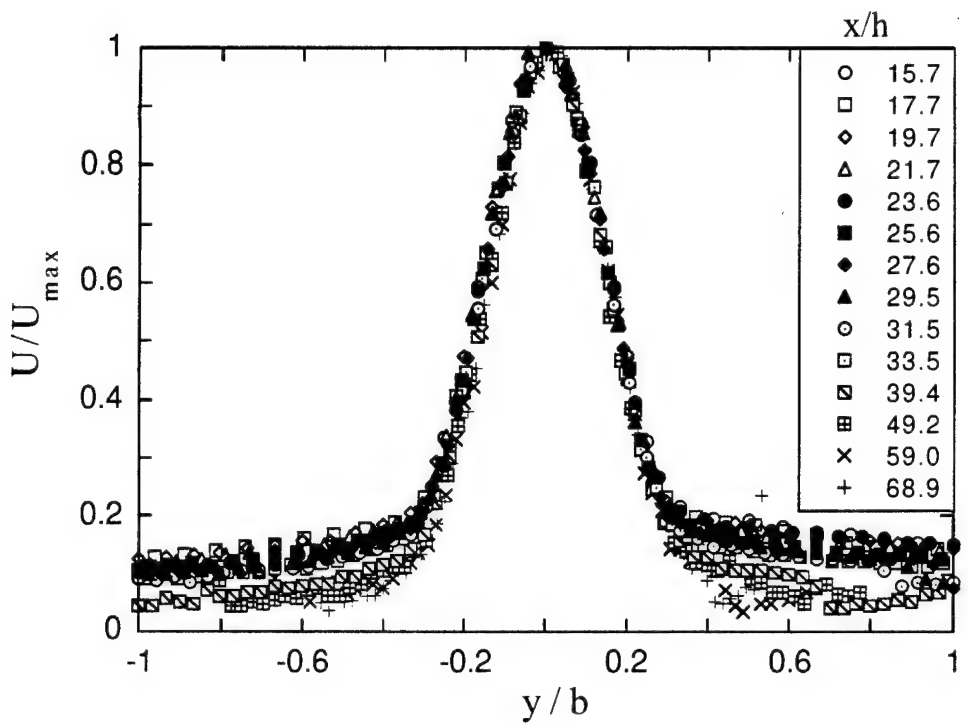


a

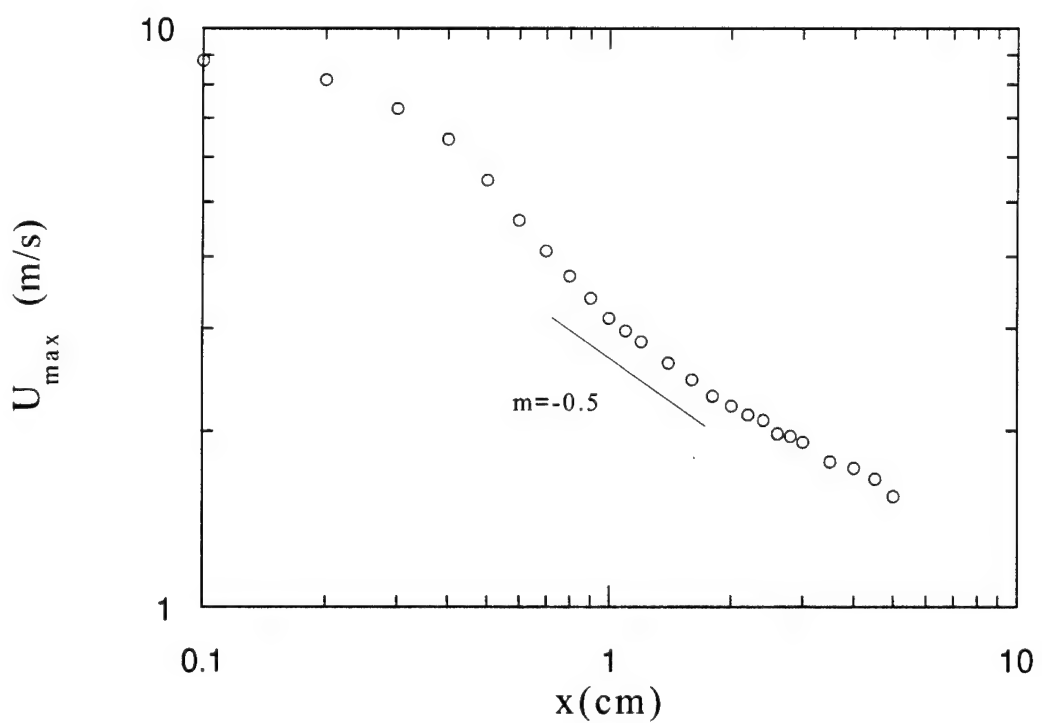


b

Figure II-1



a



b

Figure II-2

is bounded by a flexible membrane. Typical microjet orifice sizes range from 150-300 microns. Vibration of the membrane using either electrostatic or piezoelectric drive results in a nominally round turbulent air jet formed normal to the microjet orifice. A cross-section of a prototypical microjet is shown in Figure II-3. In this design, the orifice and actuator are incorporated into the same wafer. Both electrostatic and piezoelectric drive can be used in this configuration. Although only a single jet is shown in this configuration, this concept has already been extended to addressable arrays of microjets (Coe, Allen Smith and Glezer, 1995). A smoke visualization photograph of an operational microjet where the smoke is injected radially near the orifice edge is shown in Figure II-4. The piezoelectric driver is operated at its nominal 1.3 kHz resonance frequency in its first axisymmetric mode of vibration. The field of view measures 89 mm in the streamwise (x) direction and thus corresponds to nearly 500 jet diameters. The jet appears to become turbulent at or near the orifice, and spreads almost linearly with streamwise distance. Large coherent vortical structures are apparent in the far field of the jet. Jets with centerline velocities exceeding 20 m/s at a distance of 15 diameters ($Re = 1400$) have been realized. The Reynolds number of the jet based on the centerline velocity and its width at $x/D = 15$ is approximately 1400.

II.3 Shear Flow Control Using Synthetic Jets

Under support from the present Grant we have begun to demonstrate the utility of fluidic actuators in two application areas. The first application is thrust management of axisymmetric and 2-D jets and using synthetic control jets scaling one to two orders of magnitude smaller (§II.3.1). The second application area is concerned with performance modification of aerodynamic surfaces without moving controls by modifying their *apparent aerodynamic shape* (§II.3.2).

II.3.1. Jet Vectoring

The utility of millimeter-scale synthetic jets actuators for thrust vectoring of larger, centimeter-scale conventional has been recently demonstrated by Smith and Glezer (1995). In these experiments, the primary jet emanates from a rectangular conduit measuring 7.62 cm x 1.27 cm. While the lengths of the control jet orifice and the primary jet conduits are the same, the width of the control jet orifice is 25 times smaller. The jet actuator is placed near the exit plane and along the long side of the primary jet and can be rotated so that the angle between their respective centerlines can be continuously varied. In the experiments reported here, the centerlines of two jets are co-linear (Figure II-5a), the centerline velocity of the primary jet at the exit plane is 6.5 m/sec, and the ratio of the flux of

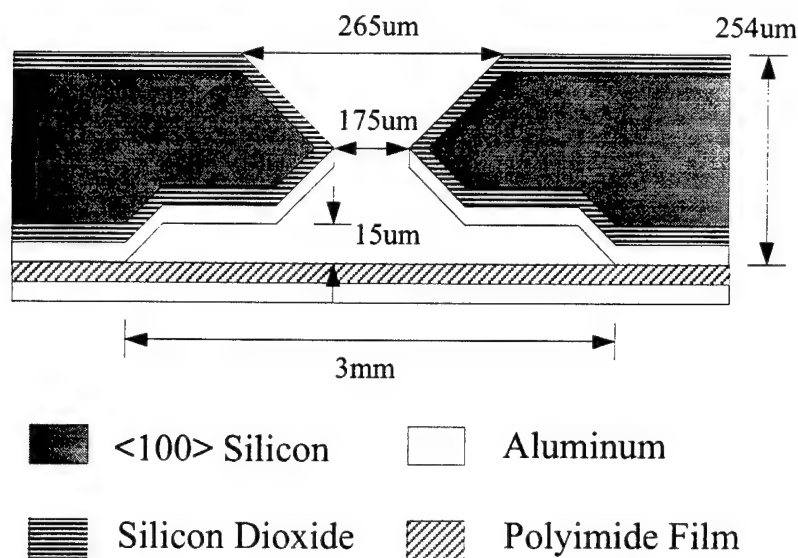
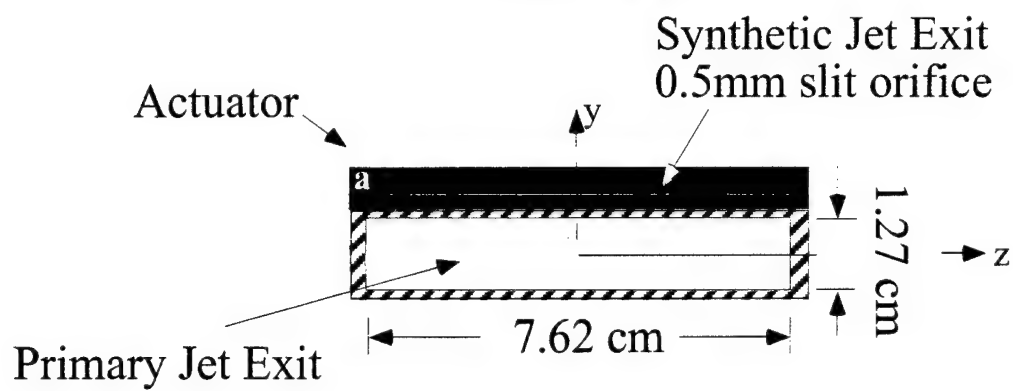


Figure II-3

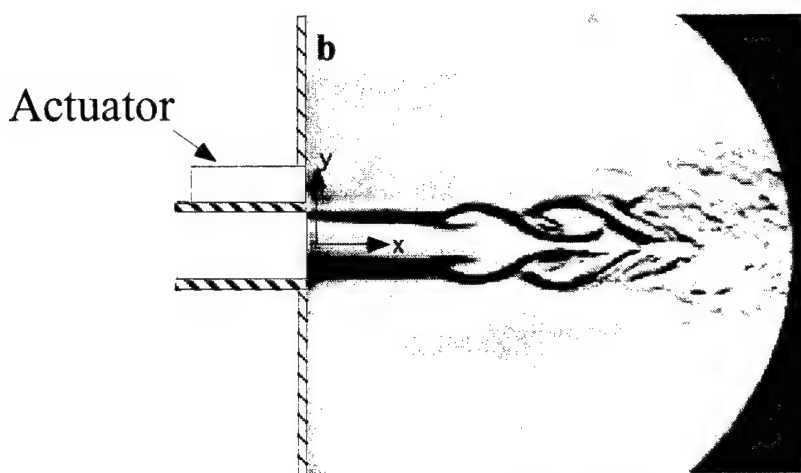


Figure II-4

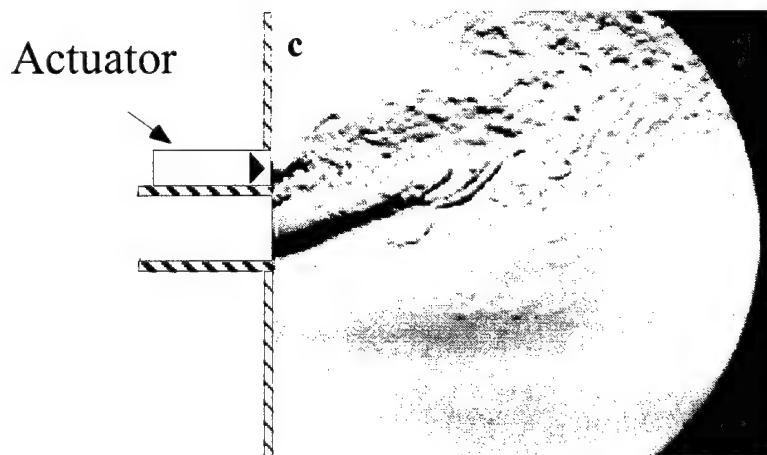
Front View



Side View



Unforced



Forced

Figure II-5

streamwise momentum per unit span between the control jet and the unforced primary jet is approximately 1/35.

The interaction between the control jet and the primary jet is demonstrated in the Schlieren photographs of Figure II-5(b, c). The unforced primary jet is shown for reference in Figure II-5b. When the actuator is activated (Figure II-5c), the primary jet is vectored upward (i.e., towards the actuator). The vectoring is a result of a Coanda effect resulting from strong entrainment and a low pressure region that are induced by the control jet as shown schematically in Figure II-6. Because the control jet entrains ambient fluid on both sides, it appears that its interaction with the primary jet leads to the formation of a Coanda surface along the dividing stream lines between the two flows.

Distributions of the streamwise and cross-stream velocity components were measured using hot-wire anemometry at a number of streamwise stations. Figures II-7a and b show profiles of the streamwise velocity component plotted in similarity coordinates for the unforced and vectored jets, respectively. The velocity profiles of the vectored jet in Figure II-7b are displaced in y so that the maximum velocity at each streamwise station lies at $y = 0$. [The present data shows that the loci of the maximum streamwise velocity in the x - y plane (x and y are the streamwise and cross-stream directions, respectively) lie on a ray that forms an angle of 28° with the x axis.] These data show that while the vectored jet is nominally self-similar along its unforced side, the forced side becomes self similar farther downstream ($x/h > 8.6$). This suggests that the vectoring is a near field effect and that once it is completed, the jet remains vectored and becomes self-similar.

The effect of the control jet on entrainment by the primary jet, is assessed from variation of the jet volume flowrate with downstream distance for the forced and unforced cases (Figure II-8). The volume flow rate of the unforced primary jet remains almost unchanged until the jet becomes turbulent and entrainment increases. In contrast, the vectored primary jet entrains substantially more fluid and its volume flow rate is over 300% larger than that of the unforced jet. The volume flow rate of the control jet is also plotted for reference and it is noteworthy that the difference in the flow rate between the forced and unforced primary jet is considerably larger than the flow rate of the control jet.

Distributions of the streamwise and cross stream velocity components in a coordinate system that is aligned with the vectored jet \tilde{u} and \tilde{v} , respectively, were measured using X-wire sensors. Figure II-9 shows distributions of \tilde{u} in the planes $x/h = 0.8$, 3.2, and 6.3 (Figures II-9 b, c, and d, respectively) and demonstrates that the cross section of the vectored jet becomes increasingly distorted with downstream distance. The inner edges of the primary jet conduit are outlined on each plot for reference. At $x/h=0.8$, the primary jet and the synthetic jet are clearly distinguishable and nominally rectangular.

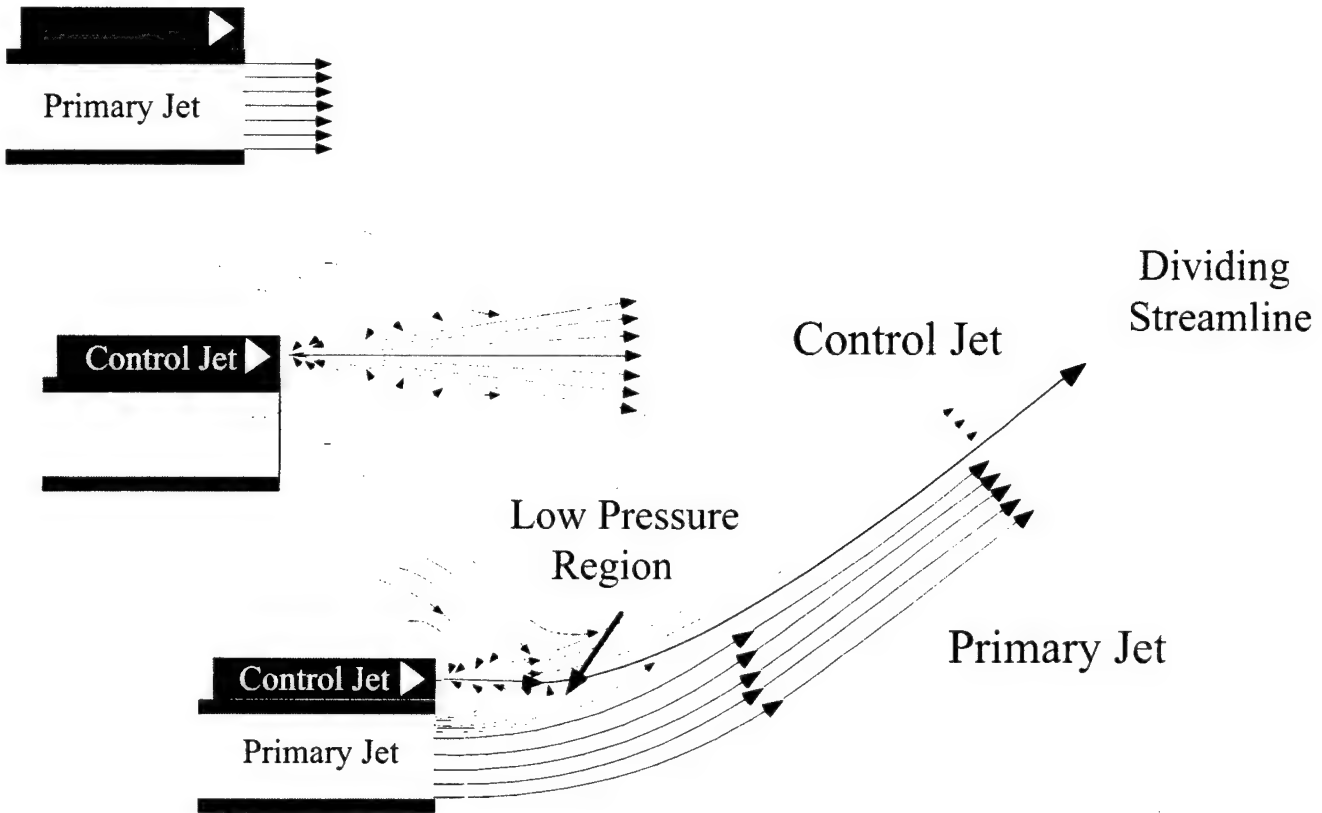


Figure II-6

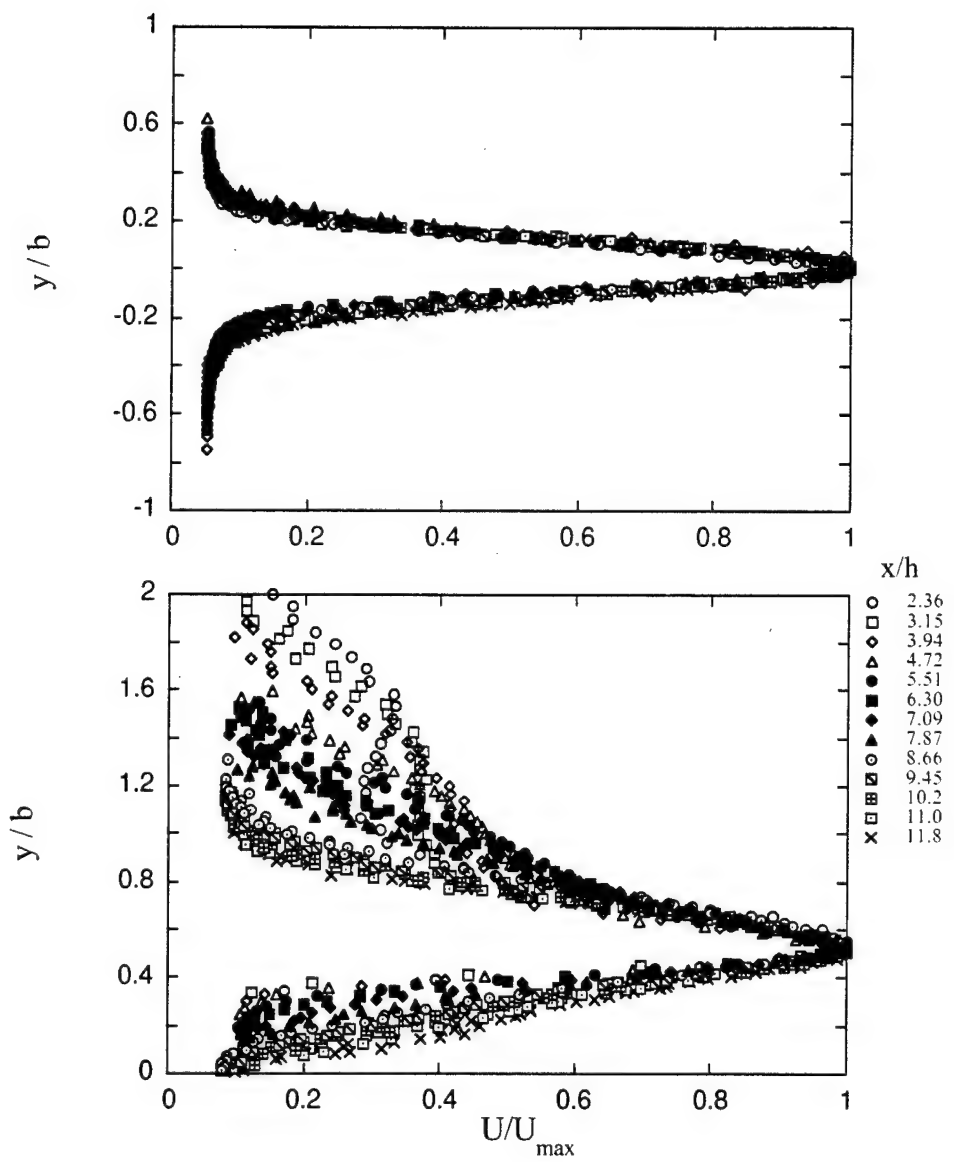


Figure II-7

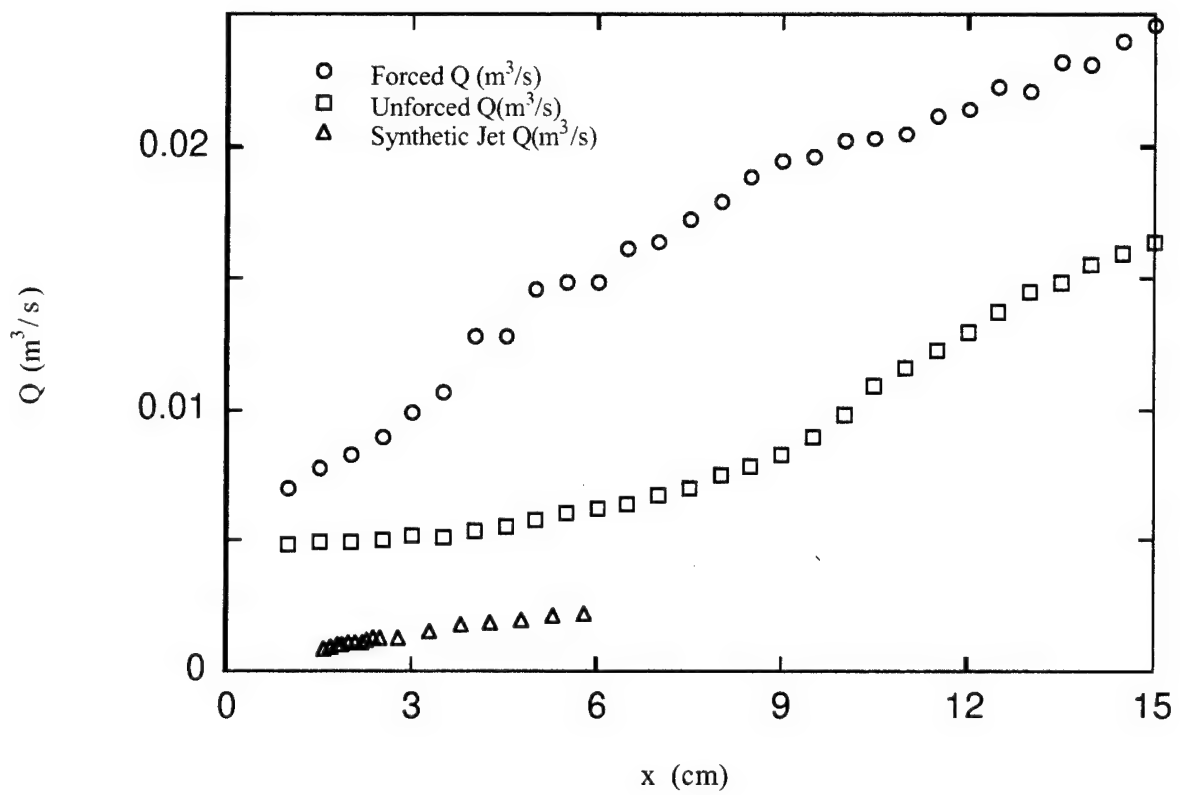
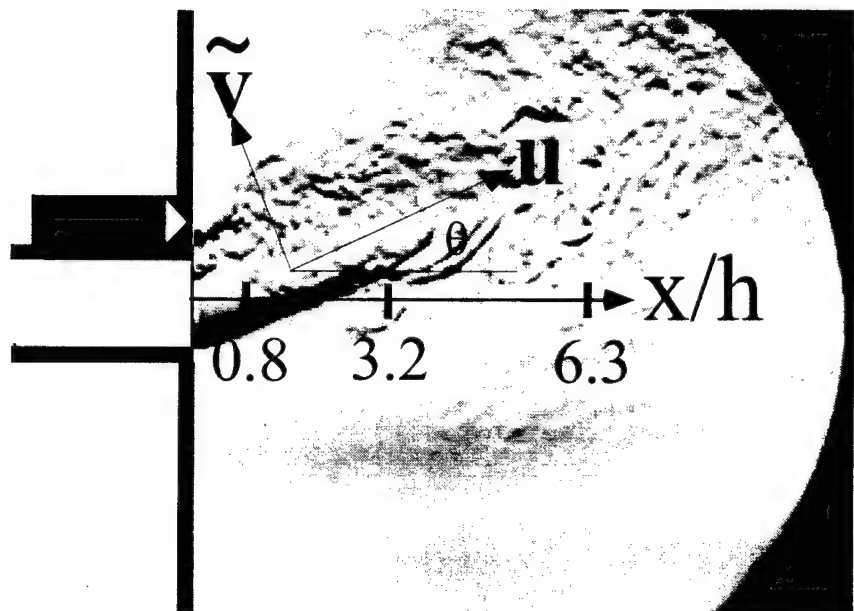
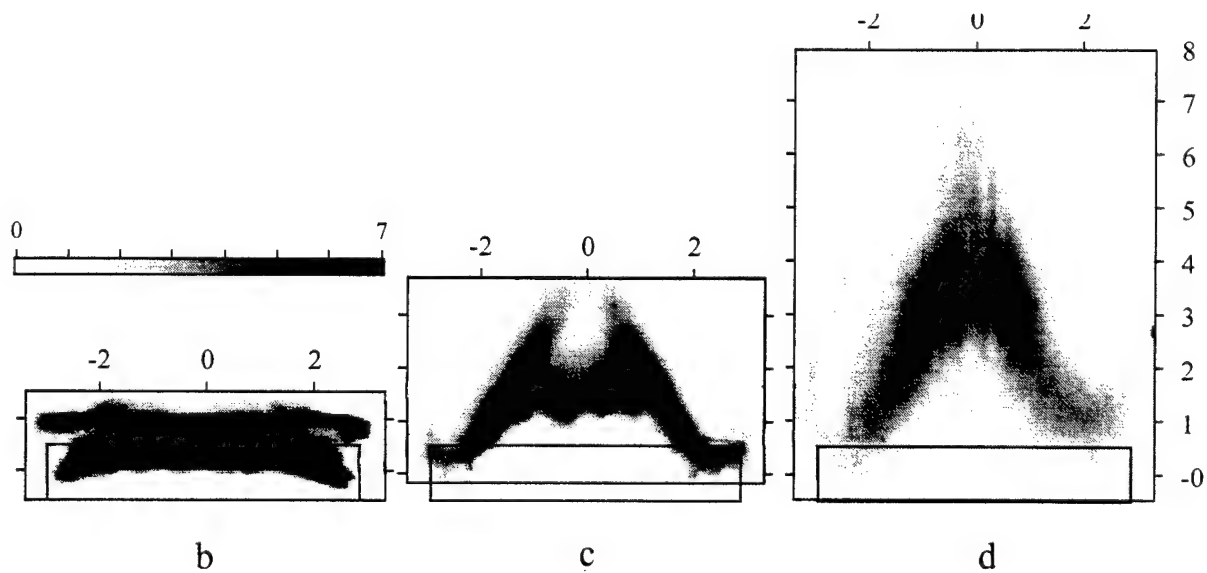


Figure II-8



a



b

c

d

Figure II-9

At $x/h = 3.2$, the two jets appear to be merged and the primary jet is distorted as a result of spanwise-nonuniform vectoring. In fact, it appears that the spanwise edges of the jet are vectored less than its center. At $x/h=6.3$, the spanwise edges of the primary jet appear to have merged and the jet cross section becomes nearly triangular.

The mean spanwise vorticity component was computed from detailed X-wire measurements of the velocity distribution in the cross stream plane $z=0$ (Figure II-10). These data show that although the lower shear layer of the primary jet is vectored, it is relatively undisturbed. However, the forcing by the synthetic jet leads to radical modification of the vorticity distribution in the upper shear layer which is substantially broader in the cross stream direction. Furthermore, as a result of the forcing, the spanwise vorticity in the upper shear layer exhibits vorticity concentrations of the opposite sign near the orifice of the synthetic jet ostensibly as a result of the formation of counter-rotating spanwise vortex pairs along the span of the primary jet. The interaction of these vortices with the predominantly single-sign spanwise vorticity in the upper shear layer leads to increase in small-scale mixing as indicated by the corresponding cross-stream distribution of the dissipation (Figure II-11).

An example of vectoring in the "push" and "pull" modes is shown in Figures II-12(a-d). The primary jet is instrumented with a synthetic jet actuator on each side of the flow duct. The unforced jet is shown in Figure II-12a for reference. In Figure II-12b, only the top actuator is operational. Its orifice approximately coincides with the exit plane of the primary jet and it is operating in the "pull" mode. The bottom actuator is operated in the push mode by placing it so that its orifice is slightly upstream of (i.e., behind) the exit plane of the primary jet. This displacement of the actuator allows the synthetic jet to bend around the duct of the primary jet due to Coanda effect and impinge normal to the primary jet. It is remarkable that entrainment by the synthetic jet is strong enough to enable to bend around the 90° corner of the primary jet duct. The resulting vectoring is shown in Figure II-12c and the angle is approximately equal to that of Figure II-12b (about 30°). Finally, in Figure II-12d, the top and bottom actuators are operating in concert and the vectoring angle of the primary jet exceeds 80° .

II.3.2. Modification of Aerodynamic Surfaces

Conventional methods for the modification of lift and drag on aerodynamic surfaces have primarily focused on delay of separation or inducement of reattachment by introducing small disturbances into the upstream wall boundary layer. Excitation methods have included external and internal acoustic excitation (Huang, Maestrello & Bryant, 1987, respectively), vibrating flaps (e.g., Neuberger & Wygnanski, 1987) and unsteady bleeding

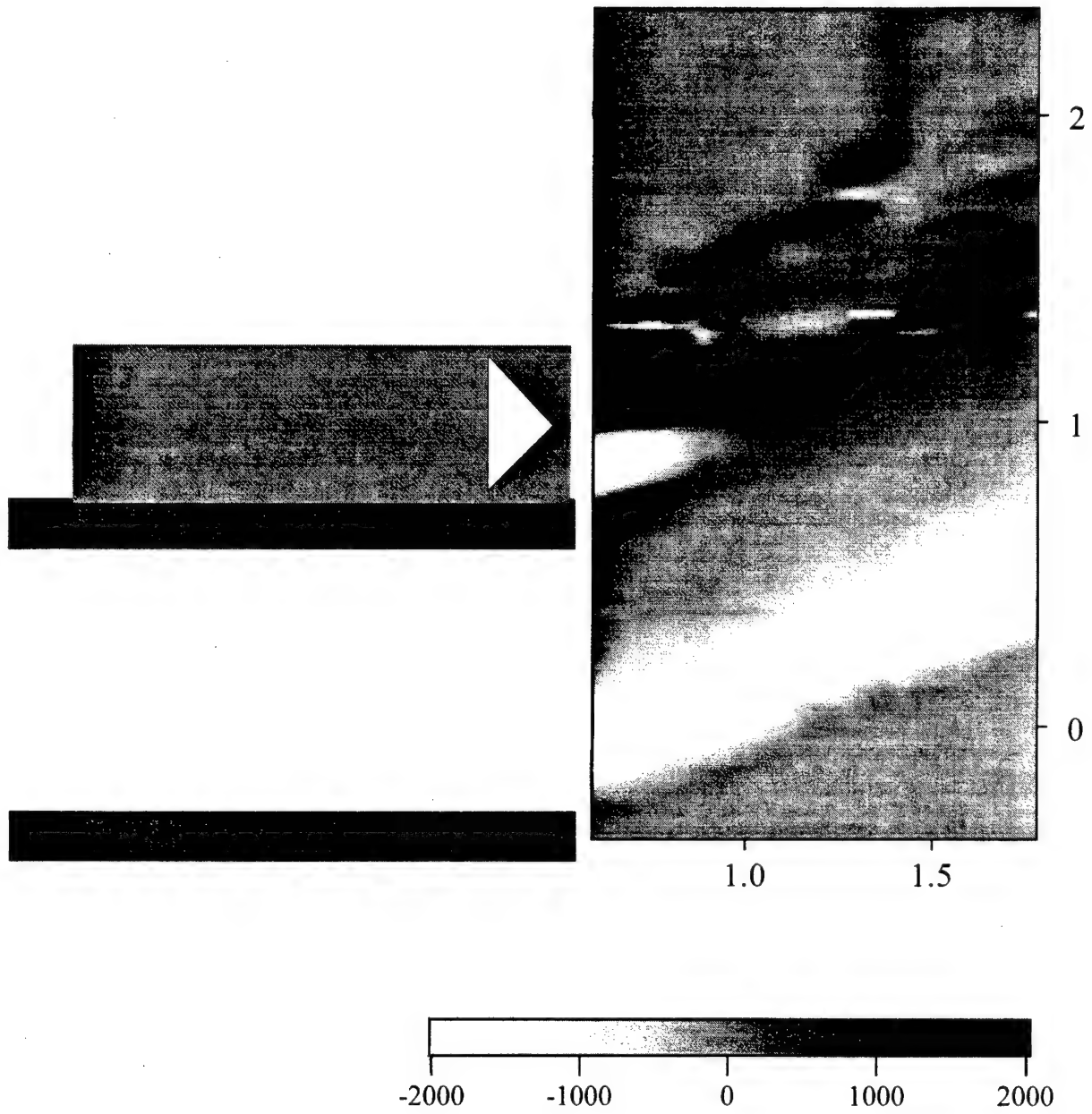


Figure II-10

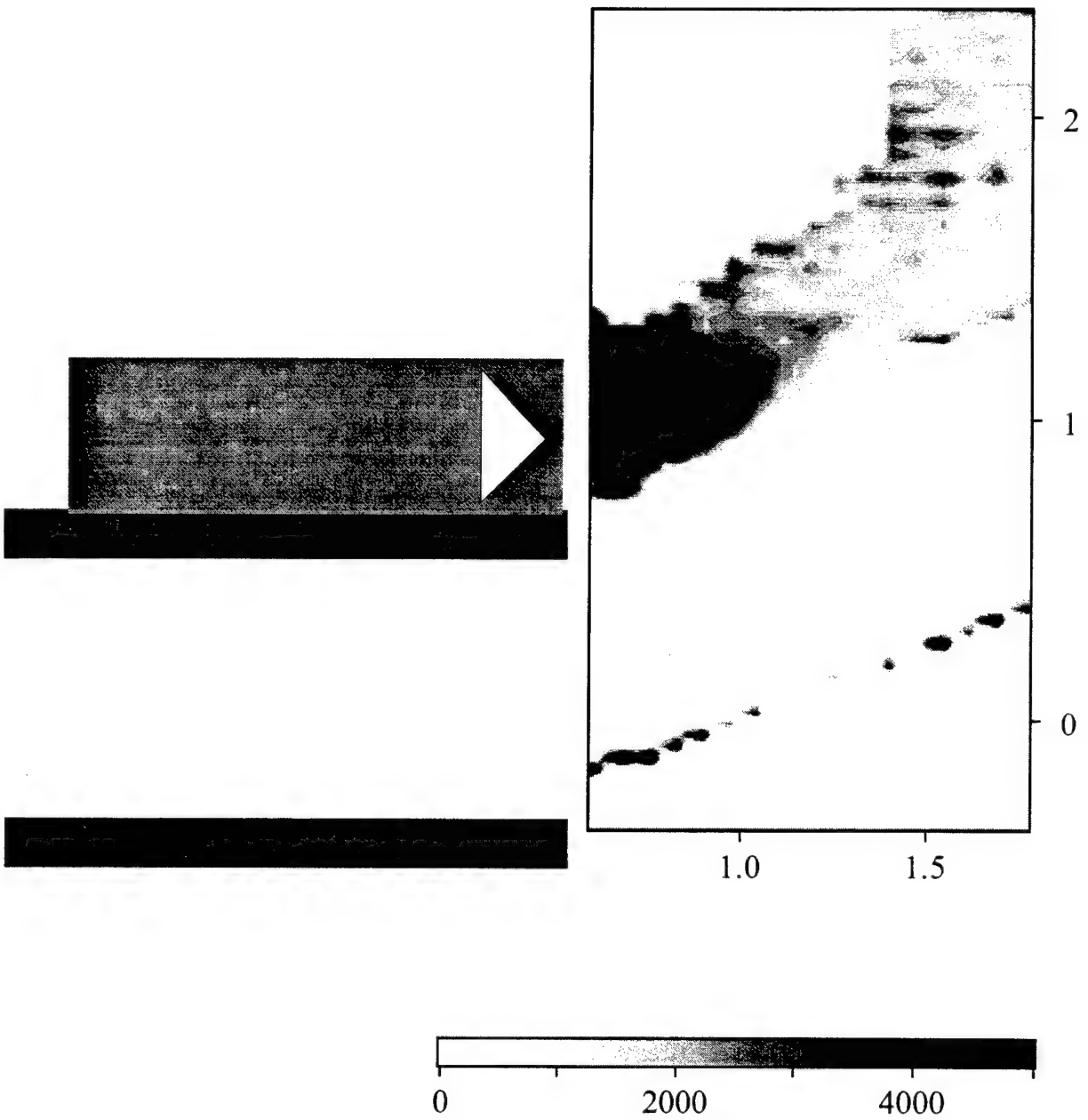


Figure II-11

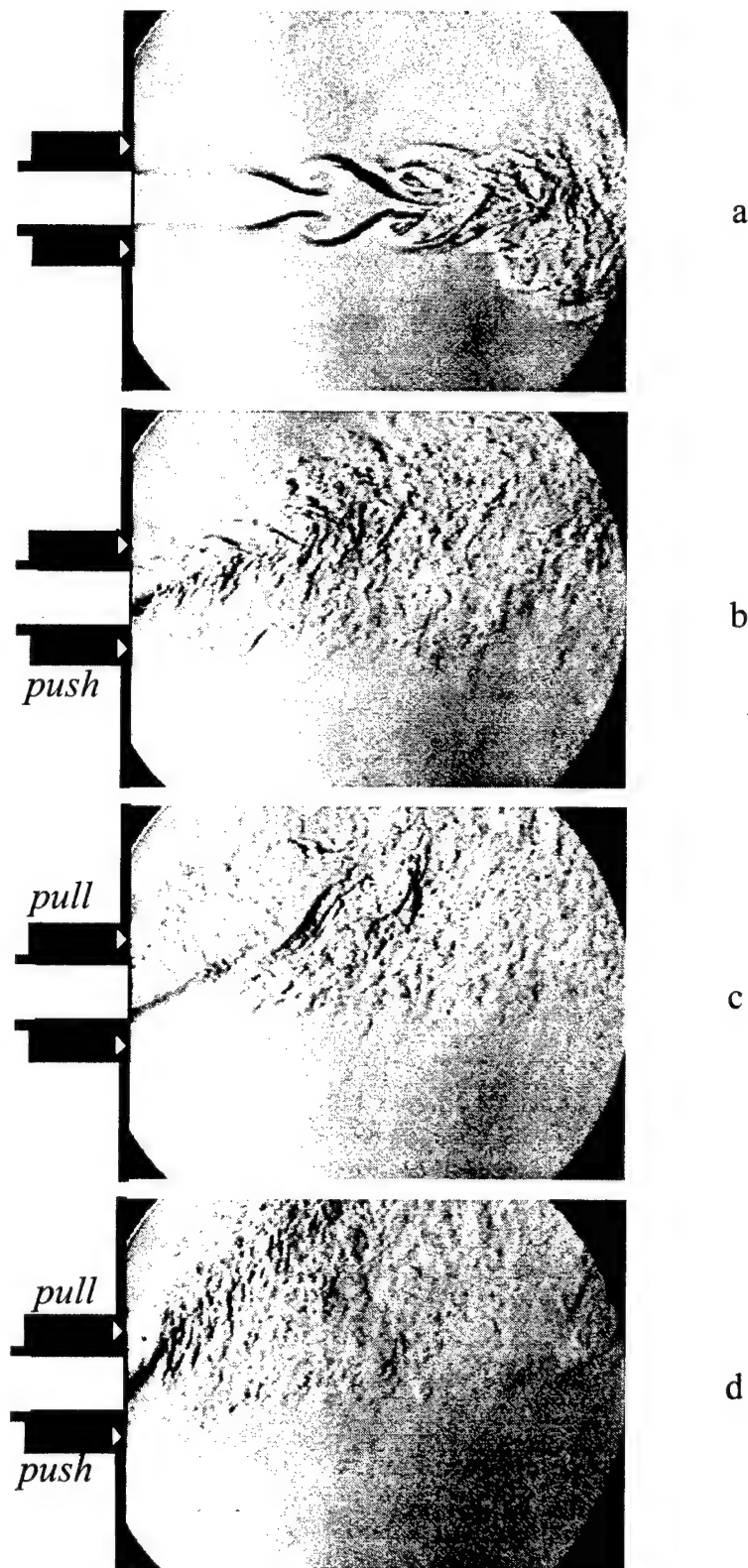


Figure II-12

or blowing (e.g., Sigurdson & Roshko, 1985, and Seifert, Bachar, Koss, Shephelovich & Wygnanski, 1993). These methods have been used with varying degrees of success and depend on the receptivity of the boundary layer to excitation within a relatively narrow bandwidth.

In contrast to these approaches, a unique feature of synthetic jet actuators is that they can effectively modify wall-bounded shear flows by creating closed recirculating flow regimes near solid surfaces that may protrude into the external flow well beyond the surface boundary layer. As discussed in §II, these closed flow regimes can be formed when the jets are placed in an embedding flow, because the jet actuators do not dispense new fluid into the flow. Thus, when synthetic jet actuators are placed near solid surfaces in wall bounded flow, they result in a change in the *apparent aerodynamic shape* of the surface; hence they can be exploited for modification of aerodynamic performance measures such as lift or drag. In particular, because the aerodynamic characteristics of an airfoil depend critically on the location of its front and rear stagnation points and on its camber and thickness, these characteristics can be altered by synthetic jet actuators *without the use of movable flaps*. Placement of jet arrays along the leading and trailing edges and along the upper and lower surfaces of an airfoil can result in displacement of its front and rear stagnation points and changes in its apparent thickness and camber, respectively. Addressable jet arrays can also be used to dynamically tailor and optimize the aerodynamic performance preventing premature flow separation and thus loss of lift.

In wind recent tunnel experiments we have demonstrated the utility of synthetic jets for the modification of the nominally 2-D flow around a cylinder. The cylinder has a diameter of 6.35 cm and a horizontal span of 74 cm. The center section of the cylinder is instrumented with a plane synthetic jet emanating radially from the shell through a flush orifice measuring 0.5 x 163 mm (Figure II-13). The cylinder can be rotated about its centerline so that the angle between the jet and the direction of the free stream in the tunnel can be continuously varied. The center segment is also instrumented with 47 pressure ports that are equally spaced around the circumference of the cylinder. Measurements of the static pressure distribution around the perimeter of the cylinder are taken using a 48-port Scanivalve and a pressure transducer. In the measurements reported here, the tunnel speed of 13.5 m/sec (the Reynolds number based on the cylinder diameter is 55,000) and the jet is issuing from the top half surface.

Figure II-14 shows the azimuthal variation (with θ) of the pressure coefficient C_p around the circumference of the cylinder with and without the presence of a synthetic jet (the jet angle θ_j is 85°). These data show that the when the jet is active, the pressure on the top surface of the cylinder in the vicinity of the jet is substantially reduced, ostensibly

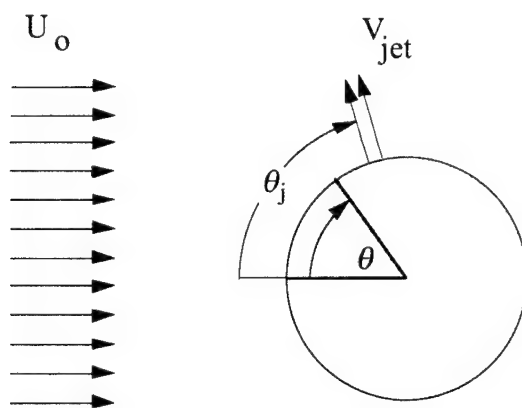


Figure II-13

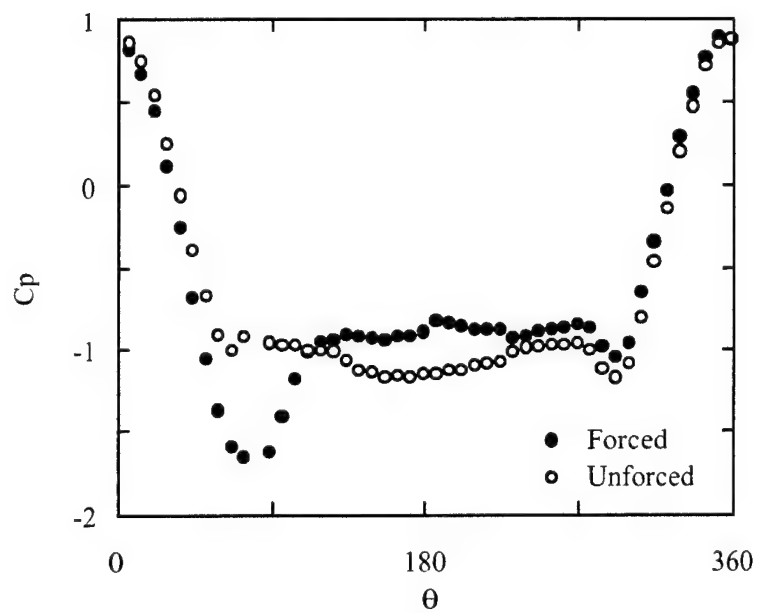
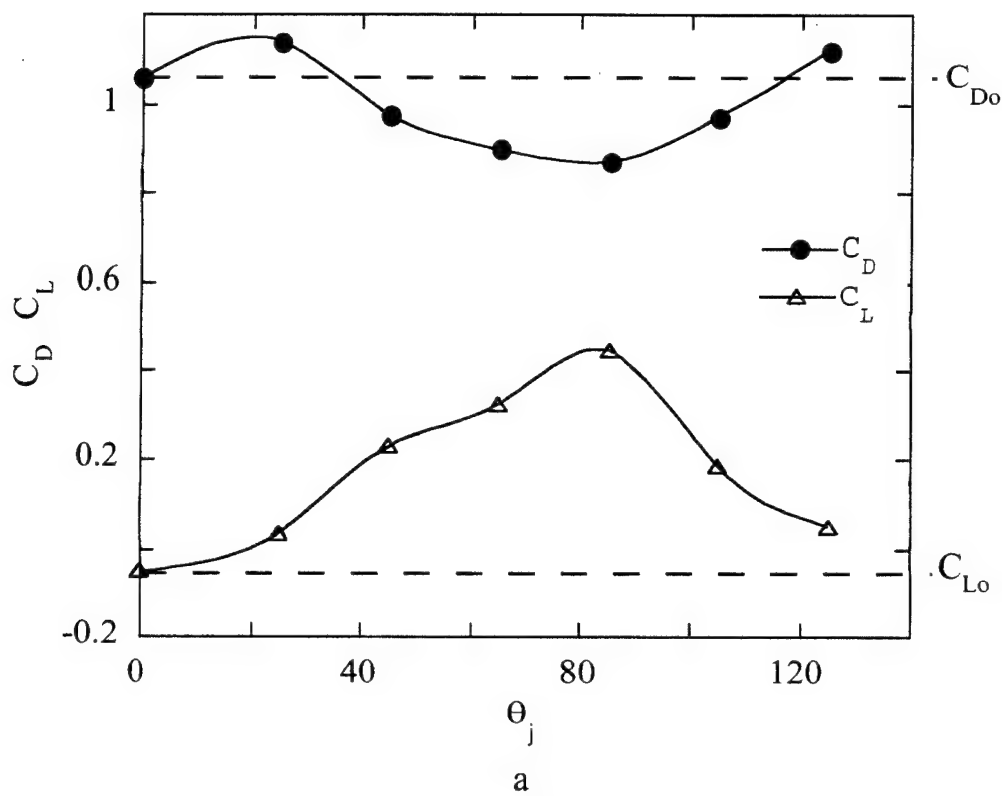


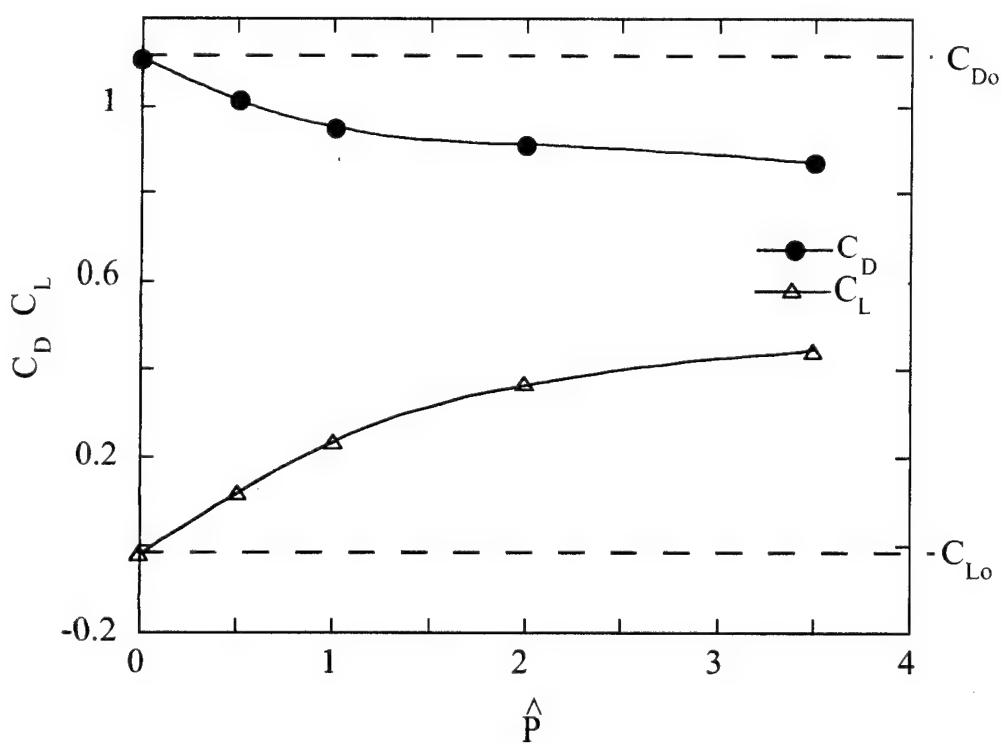
Figure II-14

owing to a corresponding change in the streamline curvature of the external flow. It is noteworthy that the change in the surface pressure distribution, in the absence of flow in the tunnel, is virtually immeasurable with the present pressure transducer. The diminution in static pressure on the top surface yields a net vertical force and thus a lift coefficient $C_L = 0.35$ (in the absence of the jet $C_L = 0.015$). This lift coefficient corresponds to an angle of attack of 3° for a NACA 63-018 symmetric airfoil (maximum lift coefficient 1.4 at an angle of attack of 13°). The jet also results in a symmetric increase (top and bottom) in the base pressure of the cylinder so that the pressure drag C_D is decreased by 23% relative to the unforced case from 1.1 (e.g., Schlichting, 1979) to 0.84.

Figures II-15a and b show the variation of C_L and C_D with jet momentum (which is adjusted by varying the amplitude of the actuator's input) and the jet angle θ_j relative to the oncoming stream, respectively. The dependence of C_L and C_D on the strength and orientation of the jet actuator clearly indicates the potential for proportional control of the cylinder's lift and drag.



a



b

Figure II-15

III. DIRECT EXCITATION OF SMALL-SCALE MOTIONS IN FREE SHEAR FLOWS

III.1. Technical Background

Mixing processes in turbulent shear flows are typically induced by a hierarchy of vortical structures of decreasing scales that evolve as a result of inherent hydrodynamic instabilities of the base flow and can be manipulated by excitation of these instabilities through the introduction of controlled disturbances at the flow boundary (Ho & Huerre, 1984). Thus, the traditional approach to the enhancement of mixing at the small-scales has relied on the manipulation of global, two-and three-dimensional instability modes of the base flow with the objective of controlling the mixing through the modification of the ensuing large-scale vortical structures (e.g., Roberts, 1985). This approach has been motivated by the notion that the smallest and largest scale turbulent motions are primarily coupled through a local cascade of momentum and energy from large to small scales until molecular mixing ultimately takes place at the smallest scales (e.g., Broadwell and Breidenthal 1982). However, an inherent disadvantage of this approach is that control of the small-scale dynamics is *indirect* and must be tailored to the dynamics of the large scales. As a result, mixing at the smallest scales is only *weakly coupled* to the control input.

Yeung, Brasseur & Wang (1994) has demonstrated that in fully turbulent flows there is, in addition to the classical cascade, another dynamical process in which large and small scales are *directly* and *bidirectionally* coupled, and that this coupling can be stimulated through coherent narrow-band forcing at either the large or small scales. The concept of long-range interactions between widely disparate scales in turbulent flows was also demonstrated experimentally by Wiltse and Glezer (1993). In these experiments, discrete wave numbers within the dissipation range of the shear layer of a square jet were excited near the jet exit plane using planar piezoelectric actuator driven at resonance. Depending on the forcing frequency, the small scale motions induced by the actuators had wavenumbers that were well within the dissipation range and one or two orders of magnitude larger than the Kolmogorov wavenumber of the base flow.

Although the spectral peak at the excitation frequency decayed downstream of the actuator, the excitation resulted in substantial broadening of the jet shear layer and the bypass of the natural evolution of the fundamental Kelvin-Helmholtz instability. Small- to large-scale coupling was achieved by the addition of discrete low-frequency sidebands (that are within the receptivity bandwidth of the base flow) to the excitation frequency. The excitation waveform is apparently demodulated by the flow and separate, low-frequency spectral components appear at the sideband frequency. This is significant because the

spectral broadening of the excitation input was restricted to high frequencies (high wavenumbers). Thus, the appearance of spectral components at low frequencies (low wavenumbers) and consequently of large-scale vortical structures, is ostensibly the result of small-scale interactions within the base flow.

In the present experiments, small-scale turbulent dissipation within a shear layer segment of an air jet is directly modified and significantly enhanced by excitation at a frequency that is only about six times larger than the Kolmogorov frequency of the base flow (i.e., the passage frequency of eddies at the Kolmogorov scale). The excitation is effected near the jet exit plane using two wedge shaped bi-nodal piezoelectric actuators.

III.2 Experimental Apparatus And Procedure

The air jet facility and the ancillary diagnostic equipment are described in detail in Wiltse & Glezer (1994). The downstream end of the facility including the wedge-shaped bi-nodal actuators that are placed near the jet exit plane and the coordinate system are shown schematically in Figure III-1. The jet emanates from a 3.81 cm (1.5 in) square and 57 cm long aluminum conduit that is centrally mounted on the downstream endplate of a cylindrical plenum tube. No contraction is used, and an azimuthally uniform bleeding gap along the perimeter of the plenum tube (Figure III-1) is adjusted until the velocity distribution across the plenum tube just upstream of the inlet of the square conduit is approximately uniform. This minimizes secondary flow at the inlet and along the corners of the square conduit and, as a result, the turbulence level at the jet exit. The jet is driven by an axial blower powered by a DC motor and jet velocities up to 20 m/sec can be realized.

The streamwise velocity component is measured using a single miniature hot-wire sensor and a constant current anemometer having a frequency response exceeding 100kHz. The hot wire probe is mounted on a computer-controlled three-axis traversing mechanism and measurements are taken in the plane $y = 0$ within the streamwise domain upstream of where the jet shear layers begin to merge. An Apple Macintosh 840AV laboratory computer system equipped with a 100 kHz A/D board is dedicated to experiment control and data acquisition. A double-pass Schlieren system is used to visualize the flow when the jet fluid is heated approximately 11°C above the ambient temperature. The Schlieren view is in the $x-z$ plane and consists of a 15.2-cm-diameter circle centered at $x = 5.08 \text{ cm}$ and $z = 0$.

In the present experiments, the time-averaged streamwise velocity and the corresponding rms velocity fluctuations on the jet centerline at $x = 0$ are $U_0 = 6.5 \text{ m/sec}$ and $u' = 0.046U_0$. The cross stream distributions of U and u' at $x = 1 \text{ cm}$ and $z = 0$ are

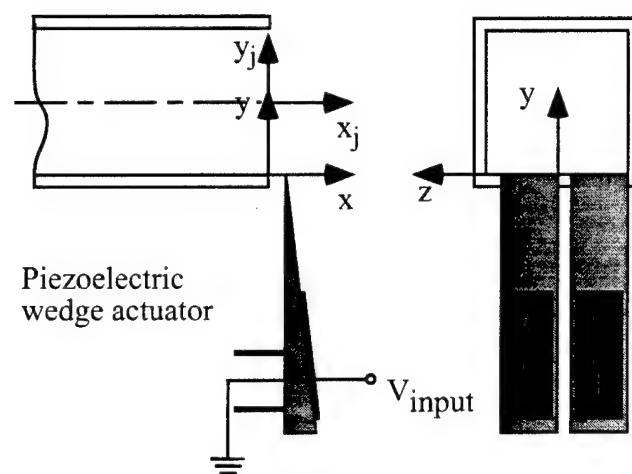


Figure III-1

shown in Figures III-2a and b, respectively. The symmetry of these distributions with respect to the jet centerline (x axis) is indicative of the flow symmetry within the square conduit and that the actuators which are mounted such that their tips are flush with the bottom surfaces of the jet conduit, have virtually no effect on the base flow when they are not activated.

A segment of the jet shear layer is forced along one side of the jet conduit 5 mm downstream from the jet exit plane by the tip motion of a pair of high-frequency bi-nodal piezoelectric cantilevered actuators (Figure III-1). Each actuator is comprised of a 6.9 cm long and 1.51 cm wide aluminum wedge where the base and tip thickness are 0.025 cm and 0.83 cm, respectively. The two actuators are mounted side by side along their long dimension and normal to the jet axis so that their tips are level with, parallel to, and approximately span the bottom inner edge of the jet conduit. A rectangular piezoceramic element operating in a shearing mode is bonded along the hypotenuse surface of the actuator wedge. When an electric field is applied across its electrodes (and normal to the axis of polarization), the actuator bends about its two nodal points. Although the resonance frequencies of the actuators are not identical, they are close enough so that the pair can be operated in concert at 5092 Hz. The peak-to-peak displacement of the actuators was approximately 0.27 mm and was adjusted so that the mean flow of the jet was virtually unchanged.

III.3 Turbulent Dissipation

The present work is primarily concerned with small-scale turbulent motions near the Kolmogorov scale. The turbulent dissipation ε is defined in terms of the fluctuating strain rate:

$$\varepsilon \equiv 2 \nu \overline{s_{ij} s_{ij}}$$

where

$$s_{ij} = \frac{1}{2} \left(\frac{\partial u_i}{\partial x_j} + \frac{\partial u_j}{\partial x_i} \right)$$

In isotropic turbulence, this reduces to

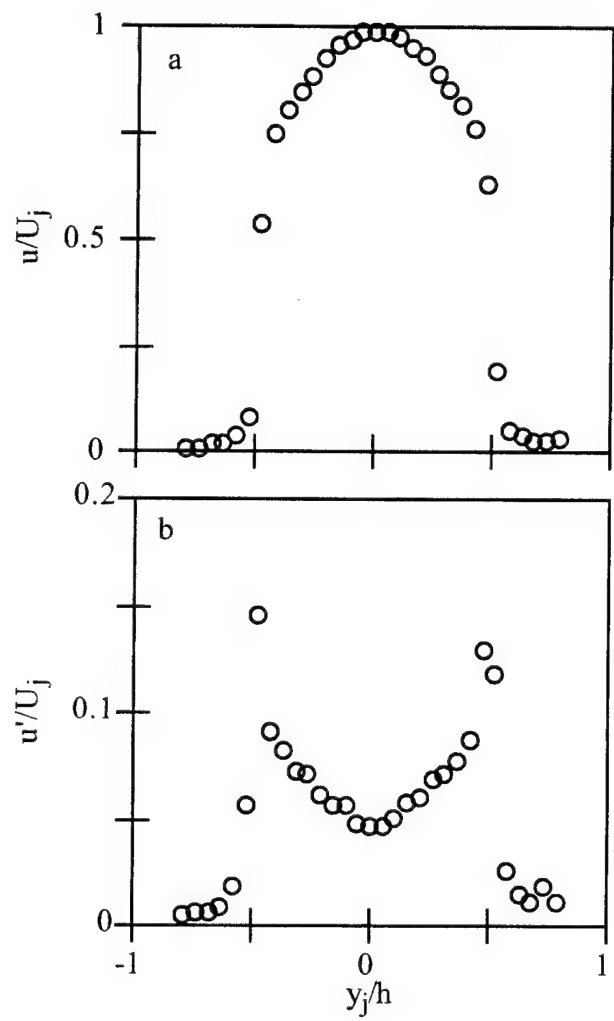


Figure III-2

$$\varepsilon = 15 \nu \overline{\left(\frac{\partial u_1}{\partial x_1} \right)^2}.$$

Using Taylor's frozen flow hypothesis, namely $\partial / \partial t = -\bar{U}_1 \partial / \partial x_1$, this can be defined in terms of a time series of velocity, as

$$\varepsilon = 15 \nu \left(\frac{1}{U_1^2} \right) \overline{\left(\frac{\partial u_1}{\partial t} \right)^2}.$$

Finally, in the present work the dissipation is corrected for the effects of finite turbulence intensity (Champagne 1978) assuming $u_1 \approx u_2 \approx u_3$:

$$\varepsilon = \varepsilon_m \left(1 + \frac{u_1^2}{U_1^2} + 2 \frac{u_2^2 + u_3^2}{U_1^2} \right)^{-1} \approx \varepsilon_m \left(1 + 5 \frac{u_1^2}{U_1^2} \right)^{-1}.$$

It is noted that the dissipation is only calculated for $u'/U_1 \leq 0.45$, for which the measured dissipation is twice as high as the corrected dissipation.

As mentioned above, in the present work the shear layer segment along the lower edge of the jet exit plane is forced at a frequency that is 2π higher than the Kolmogorov frequency of the base flow f_K (i.e., the passage frequency of eddies at the Kolmogorov scale η). The Kolmogorov scale (and hence f_K) depend, among other things, on the speed of the mean flow. Since the forcing frequency is fixed at the resonance frequency of the piezoelectric actuators (5092 Hz), it is necessary to match f_K to the resonance frequency of the actuator by adjusting the flow speed. The mean centerline velocity was iteratively chosen to be $U_0 = 6.5$ m/s. Figure III-3 shows the Kolmogorov frequency f_K for $2 \text{ cm} \leq x \leq 10 \text{ cm}$ for the unforced flow. Also shown for reference is the resonance frequency of the piezoelectric wedge actuator v_f . The Kolmogorov frequency is close to the actuator frequency throughout the streamwise domain of measurement. As will be shown below, high frequency excitation will significantly enhance the turbulent dissipation; hence this plot of f_K is accurate for the unforced flow only.

Schlieren photographs in the x-y plane of the unforced and forced jet are shown in Figures III-4a and b, respectively. The Schlieren view is a circle of diameter 15.24 cm centered at $x = 5.08$ cm and includes silhouettes of the jet conduit and of the actuator pair. The top and bottom shear layers of the unforced jet (Figure III-4a) appear to be turbulent, spread linearly with downstream distance and merge on the jet centerline at approximately

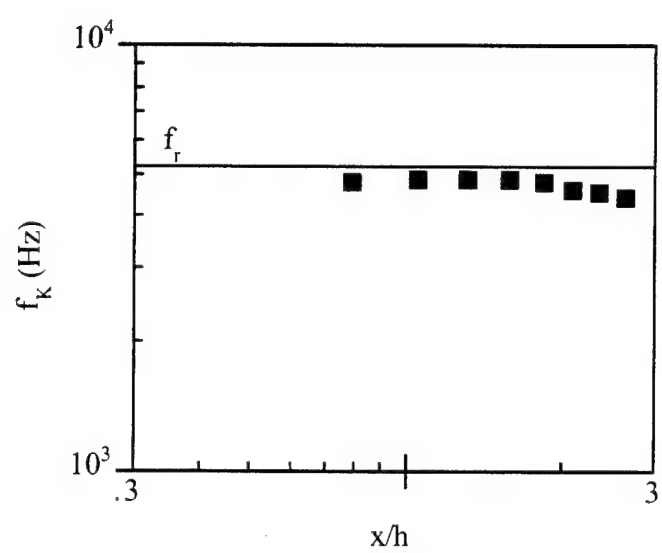


Figure III-3



Figure III-4

$x = 2.5D_e$. The streamwise domain of measurement ($1 \text{ cm} < x < 10 \text{ cm}$) is marked for reference, and the Reynolds number Re_θ of the jet shear layer (based on the mean velocity of the jet and the momentum thickness of the shear layer) varies from 875 at $x = 1 \text{ cm}$ to 1730 at $x = 10 \text{ cm}$. It is remarkable that global features of the flow remain virtually unchanged when the bottom shear layer is forced at the Kolmogorov frequency ($v_f = 5092 \text{ Hz}$). It appears that the mismatch between the unstable frequencies of the shear layer (nominally below 50 Hz) and the excitation frequency precludes global modifications of the mean flow such as spreading rate of the forced shear layer and induced instabilities of the jet column. The characteristic length scale of the eddies that are induced by the motion of the actuator is about $\lambda_f = 0.6 \text{ mm}$ and cannot be resolved with the present optical setup.

Figures III-5(a-c) show cross stream distributions in the plane $z = 0$ of the mean streamwise velocity and r.m.s. velocity fluctuations, and of the turbulent dissipation per unit mass, respectively, for the unforced flow (top) and the forced flow (bottom) for ten equally-spaced streamwise stations between $x = 1$ and 10 cm . As discussed above, the distributions of $U(y)$ and $u'(y)$ demonstrate that the mean flow is almost unaffected by the forcing. The primary differences between the forced and the unforced flows are evident for $x > 5 \text{ cm}$, where the shear layer of the forced flow is somewhat broader (at $x = 10 \text{ cm}$, $\theta = .44 \text{ cm}$ and $.45 \text{ cm}$ for the unforced and forced flow, respectively) and its peak levels of u' decrease faster with downstream distance. By contrast to the distributions of U and u' , there is an increase of 1 to 2 orders of magnitude in the time-averaged dissipation ϵ (Figure 7c) within the forced segment of the jet shear layer compared to the unforced flow (note that the dissipation within the forced flow is plotted on a different scale than for the unforced flow). While in the unforced flow the maximum dissipation within the jet shear layer is almost invariant with downstream distance ($\epsilon = 65 \text{ m}^2/\text{s}^3$ and $45 \text{ m}^2/\text{s}^3$ at $x = 1$ and 10 cm , respectively), in the forced shear layer, the peak levels of the dissipation decrease significantly from $1370 \text{ m}^2/\text{s}^3$ at $x = 1 \text{ cm}$ to $90 \text{ m}^2/\text{s}^3$ at $x = 10 \text{ cm}$.

Based on classical notion of the receptivity of shear flows to external excitation, it might be expected that the jet shear layer is not receptive to excitation at frequencies that are higher than any frequency that is normally amplified by the flow, and that the induced disturbances are rapidly attenuated immediately downstream of the actuator. In the present experiments, the amplitude of the streamwise velocity perturbation at the tip of the actuator (at a peak-to-peak tip displacement of 0.27 mm) is 4.3 m/s and the forcing is apparently introduced through localized modulation of the mean shear (or vorticity). The effect of the forcing is shown in velocity spectra $S(v)$ of the forced and unforced flow that are measured in the center plane $z = 0$ at $y = 0$ at $x = 5 \text{ cm}$ (about $80\lambda_f$) and 10 cm (about $160\lambda_f$) (Figures III-6a, and b). For clarity, the spectra of the forced flow are displaced 3 decades

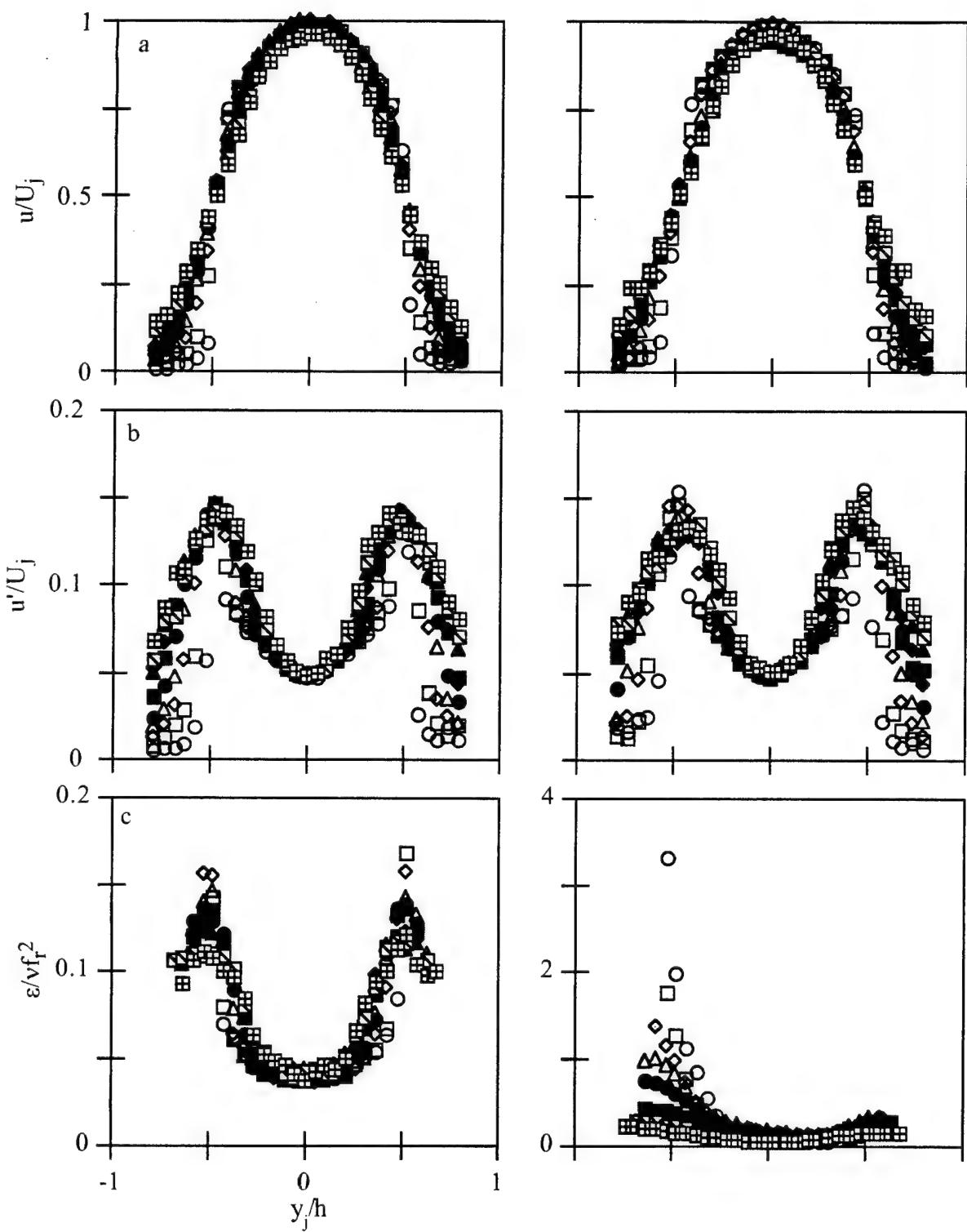


Figure III-5

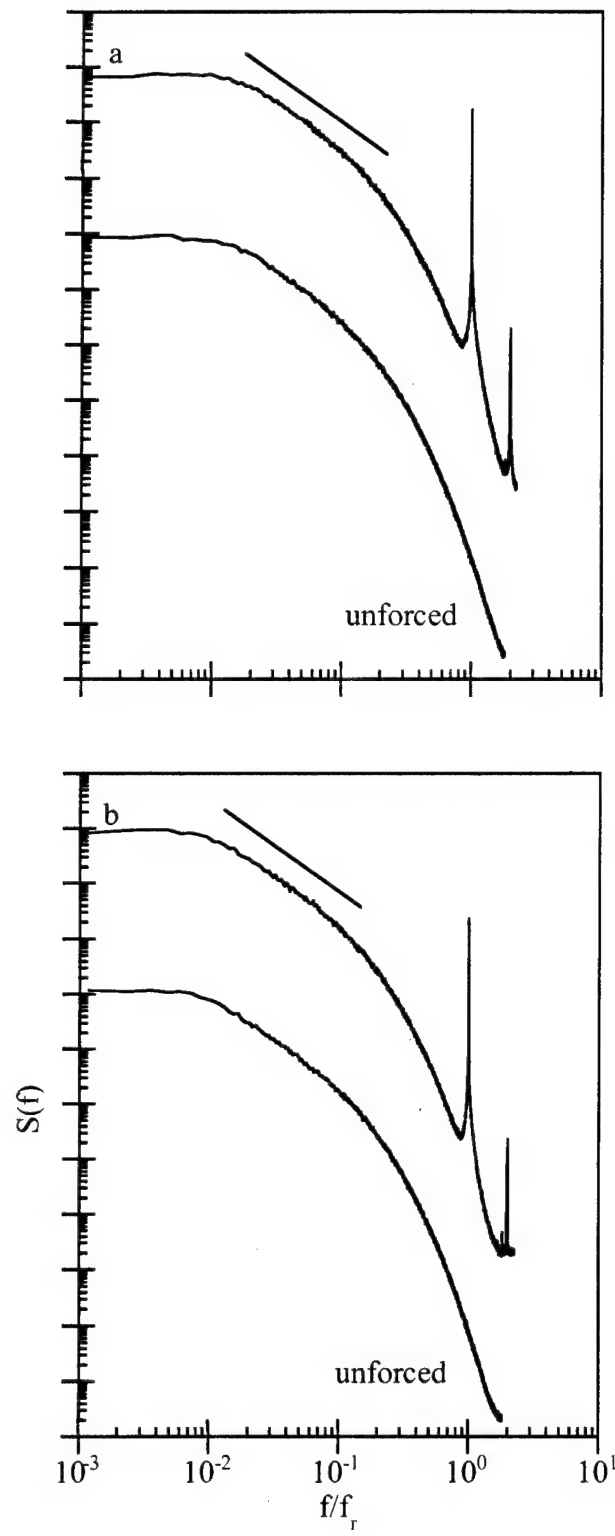


Figure III-6

upwards. Also shown for reference is a line with slope $-5/3$ corresponding to the conventional inertial subrange of fully-developed turbulent flows. There is no question that the excitation introduces a sharp increase in the amplitude of a frequency band centered around the excitation frequency ($4000 \text{ Hz} \leq v \leq 7000 \text{ Hz}$ at $x = 5 \text{ cm}$). It is noteworthy that at $x = 10 \text{ cm}$ (corresponding to approximately $160\lambda_f$), the power at the spectral peak of the excitation frequency decreases only by an order of magnitude and is still 4-5 orders of magnitude above the corresponding spectral peak of the unforced flow. Other data have shown that this peak is still discernible in the flow well downstream of the present domain of measurement.

The corresponding dissipation spectra $D(v)$ (Figures III-7a and b for $x = 5$ and 10 cm , respectively) show features analogous to the power spectra of the velocity. The effect of the forcing (as can be seen from the pairs of plots at either streamwise station) is to increase the level of dissipation at frequencies near that of v_f while slightly reducing it at lower frequencies (wavenumbers). This diminution is more apparent at $x = 10 \text{ cm}$. It is important to realize that, since this is a log-log plot, the total power in the narrow, high frequency peak can actually be quite significant. Again this peak is apparent at least to $x = 10 \text{ cm}$, although its maximum is about an order of magnitude lower than at $x = 5 \text{ cm}$, and its peak is somewhat narrower as well.

As was mentioned above, high-frequency excitation significantly increases the turbulent dissipation ϵ throughout the measurement regime. This can be effectively seen in time-averaged x - y grayscale raster plots of the dissipation ϵ . Figures III-8a and b show $\epsilon(x,y)$ for the unexcited and excited flow, respectively. The unforced flow is plotted from $0 \leq \epsilon \leq 140 \text{ m}^2/\text{s}^3$ and the excited flow is plotted from $0 \leq \epsilon \leq 1400 \text{ m}^2/\text{s}^3$. Clearly, high-frequency excitation significantly increases the dissipation throughout the streamwise domain of measurement. Also notice the increase in dissipation in the upper (unforced) shear layer of the excited flow, owing to acoustic excitation from the actuator. The upper lip acts as a point of receptivity for the acoustic excitation.

The streamwise variation of the dissipation within the unforced and forced shear layer along $y = 0$ (in the center plane $z = 0$) is shown in Figure III-9. In a fully developed turbulent shear flow, the dissipation should scale as $\epsilon \sim x^{-1}$. However, the dissipation in the unforced flow asymptotes to $x^{-0.5}$ ostensibly because the Reynolds number of the unforced shear layer is relatively low (at $x = 10 \text{ cm}$ $\delta \approx 1.5 \text{ cm}$, $\Delta U = 6.5 \text{ m/s}$ and thus $Re_\delta = 6000$). The striking feature of Figure III-9 is that the dissipation within the forced flow at $x = 1 \text{ cm}$ ($x/\lambda_f \approx 16$) increases by more than an order of magnitude relative to the unforced flow. Further downstream ($x \approx 4 \text{ cm}$), the streamwise gradient (in the log-log plot) of the dissipation within the forced flow becomes more negative and finally for

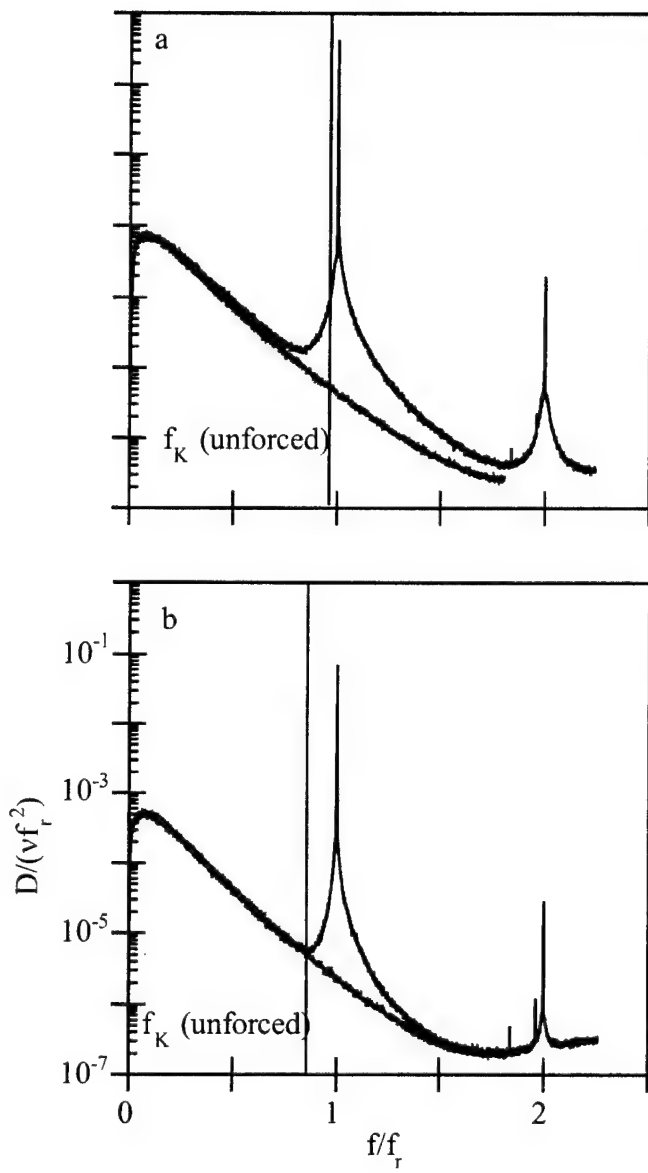


Figure III-7

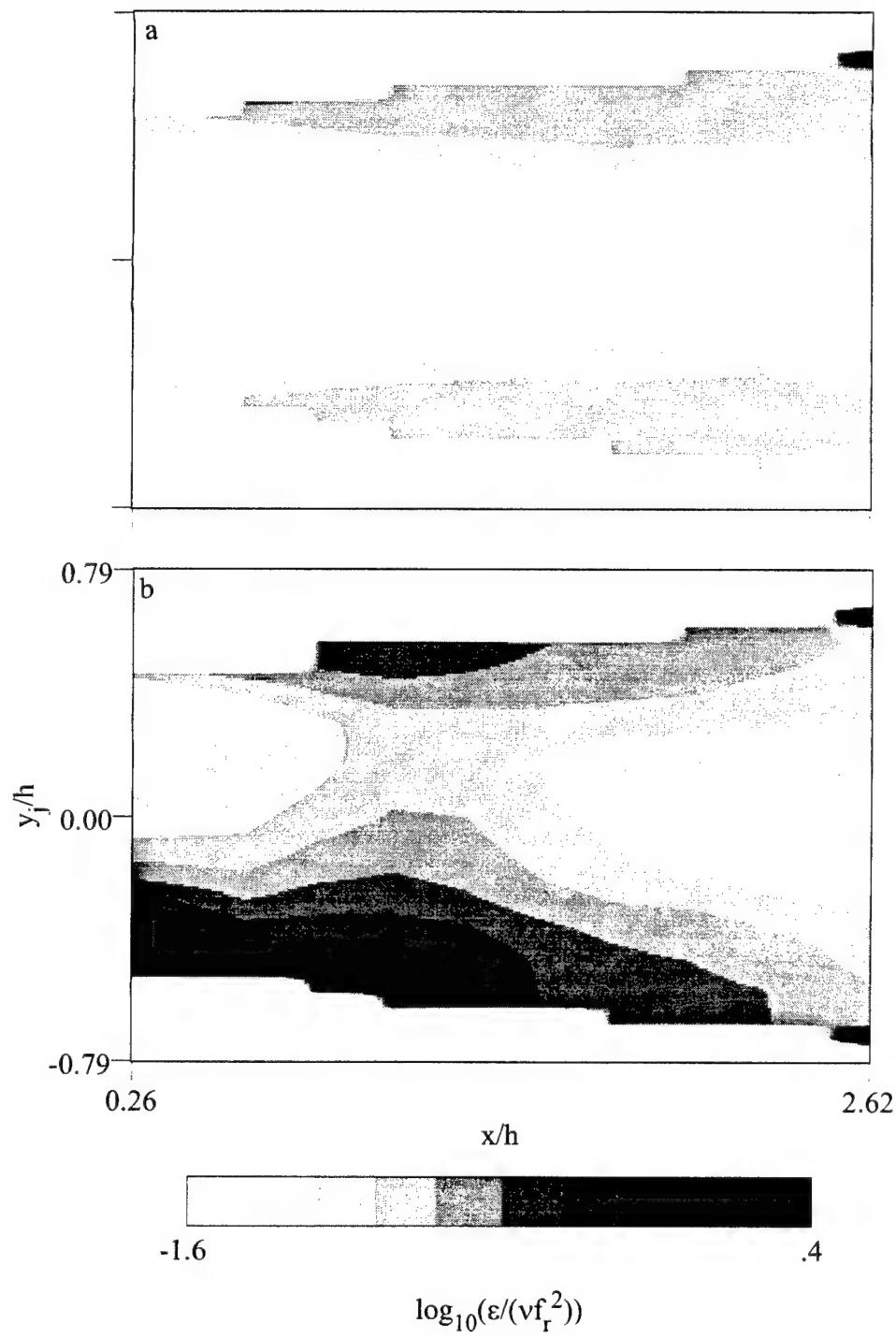


Figure III-8

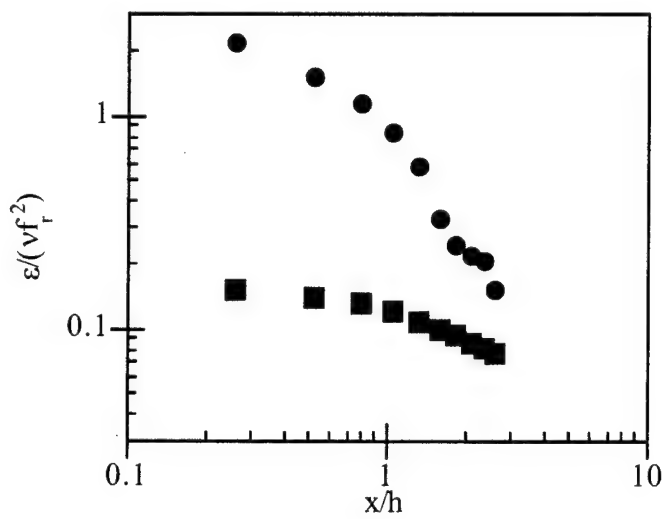


Figure III-9

$x \geq 7$ cm, ϵ asymptotes to $x^{-0.5}$ but at a level that is about 2 times higher than in the unforced flow.

Figures III-10a and b show grayscale raster images of the time-averaged turbulent kinetic energy (TKE) $u'^2(x,y)$ for the unexcited and excited flows, respectively. With the large increase in dissipation shown in figures III-8 and III-9, one would expect a corresponding *decrease* in turbulent kinetic energy relative to the unforced flow. Figure III-10 shows that this is indeed the case. Although there is an increase in the total TKE at upstream locations (in particular, the layer appears to be wider when the flow is excited), there is a decrease in TKE for $x \geq 4$ cm. In particular, forced flow exhibits a dearth of turbulent kinetic energy in the region $4 \text{ cm} \leq x \leq 7 \text{ cm}$. This region coincides with the region in Figure III-9 where the dissipation drops precipitously. Indeed, the two figures taken together suggest that the flow is "starved" of TKE from $4 \text{ cm} \leq x \leq 7 \text{ cm}$, and thus, there being less TKE to dissipate, the value of ϵ correspondingly decreases sharply. Of greatest interest is the fact that the levels of turbulence are reduced with increasing x . Further, it must be noted that the turbulent kinetic energy has been dissipated, not just transported in the cross stream direction. The width of the shear layer is approximately the same in the forced and the unforced cases.

Figure III-11 shows the streamwise variation of the turbulent kinetic energy u'^2 within the unforced and forced shear layer along $y = 0$ (in the center plane $z = 0$). The forcing results in faster streamwise dissipation of turbulent energy downstream of the actuators. It is interesting to note that although the actuators add energy to the flow, at the end of the streamwise domain considered here (i.e., $x = 10$ cm), the total turbulent kinetic energy at the point of measurement is actually reduced by approximately 16% relative to the unforced flow. It appears that when energy is added to the flow within the high wavenumber part of the equilibrium range of wavenumbers it leads to an accelerated diminution in the total turbulent kinetic energy ostensibly due to enhanced transfer to the viscous scales. Since the effect of the dissipation on the turbulent kinetic energy is cumulative, the difference in kinetic energy between the excited and unexcited flow increases with downstream distance. The streamwise gradient of turbulent kinetic energy is smaller (i.e., **more negative**) in the forced flow (nominally $-0.034 \text{ m}^2/\text{s}^2/\text{cm}$) than in the unforced flow (nominally $-0.012 \text{ m}^2/\text{s}^2/\text{cm}$).

One of the intriguing effects of direct small-scale excitation is that the addition of energy at the smallest scales apparently alters the dynamics of energy cascade across a broad range of wavenumbers that varies by as much as three orders of magnitudes. The present measurements have shown that direct small scale excitation leads to enhanced transfer of energy from the large scales to the small scales. This can be shown by

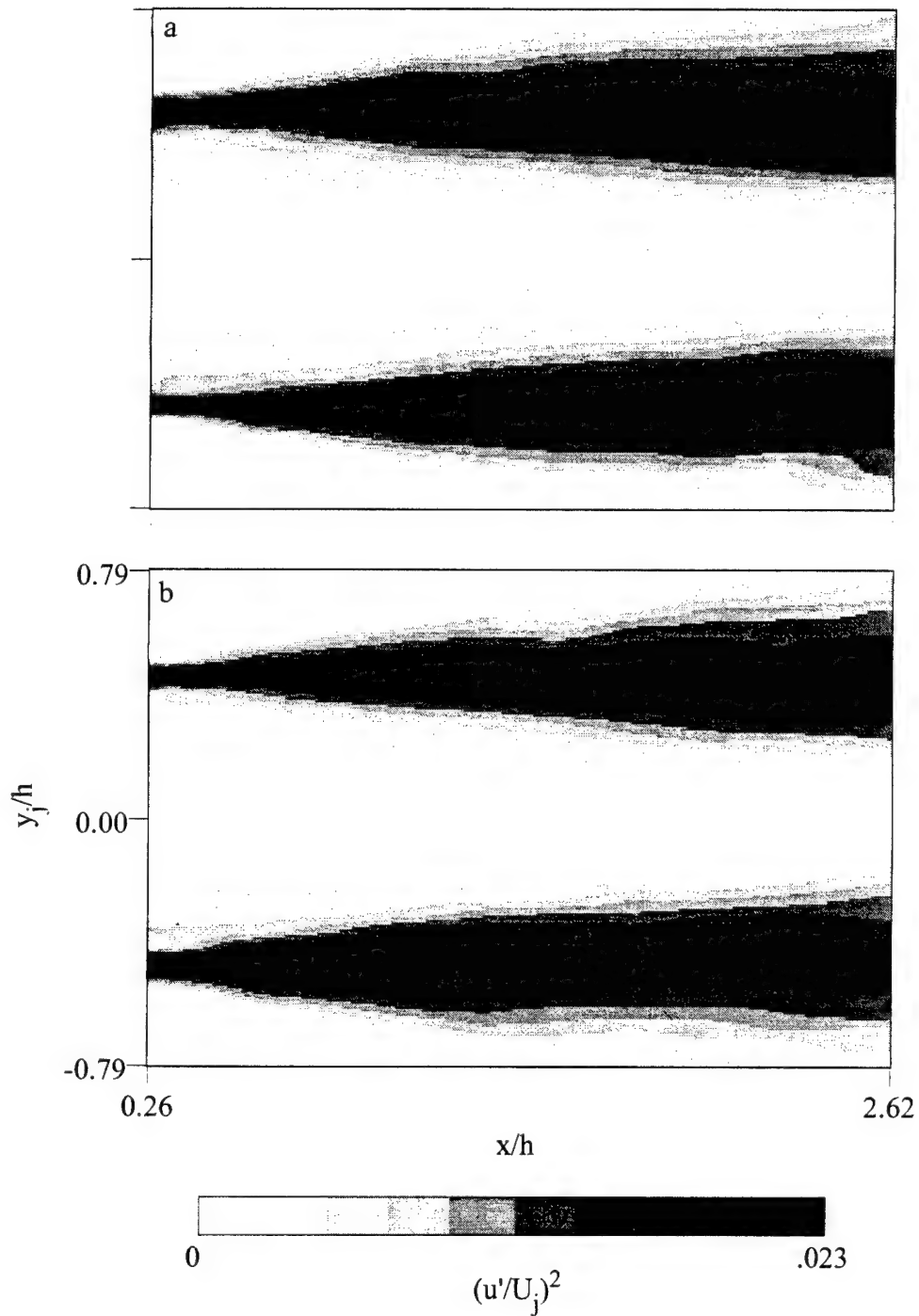


Figure III-10

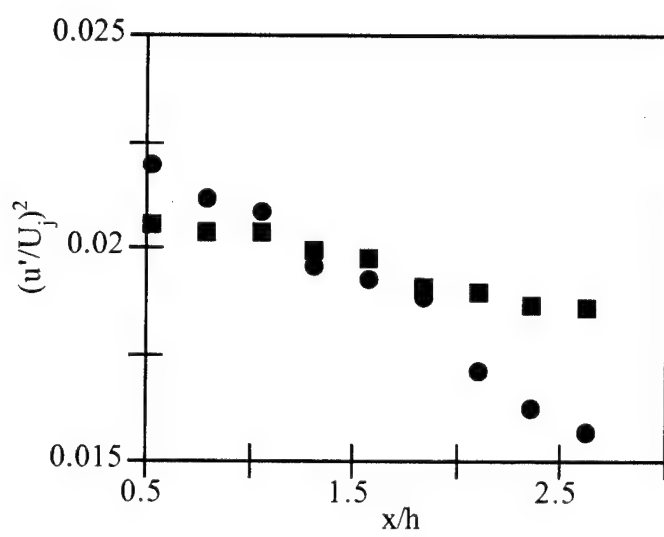


Figure III-11

comparing corresponding components of the power spectra of the forced and unforced flow at a given streamwise station. Figure III-12 ($x = 1$ cm, using black and gray curves, respectively) shows that there are two important differences between the two spectra: first, there is more power in spectral components of the forced flow above 230 Hz, even though the excitation is effected at frequencies above 5 kHz, and second, the energy in spectral components of the forced flow that are below 230 Hz is lower than in corresponding components in the unforced flow. The reduction in the magnitude of spectral components at low frequencies suggests that the forcing induces coupling (or long-range interactions) between small and large scales within the flow and thus leads to acceleration of the conventional energy cascade and to diminution in energy associated with the large scales. Such long-range coupling was investigated numerically by Yeung, Brasseur & Wang (1995). The apparent acceleration of the energy cascade is accompanied by an increase in the magnitude of spectral components within a frequency band having a lower bound at a crossover frequency (230 Hz at this streamwise location) that is at least an order of magnitude smaller than the excitation frequency. This effectively increases the inertial subrange.

Figures III-13(a-d) show the difference between the power spectra of the forced and unforced flow $\Delta S(v)$ at $x = 1, 4, 7$, and 10 cm, respectively. The difference is normalized by the total spectral power u'^2 of the unforced flow at the point of measurement. The black and gray curves represent regions where there is more energy in spectral components of the forced ($\Delta S > 0$) and unforced ($\Delta S < 0$) flow, respectively.

As discussed above, a result of the forcing, ΔS changes sign (from negative to positive) around 230 Hz, immediately downstream of the actuator (Figure III-13a). Although the forcing is introduced at the discrete frequency of 5092 Hz, the spectral power in all frequencies $v > 230$ Hz is significantly higher and thus it is apparent that high frequency excitation alters the turbulent energy cascade. Typically, the inertial subrange ends (and the slope of the spectrum begins to roll off from $m = -5/3$) at wavenumbers at which the strain rate is limited by viscosity, at wavenumbers an order of magnitude lower than those corresponding to the Kolmogorov scale. In this case, however, the forcing greatly increases the strain rate so that the roll off of the spectrum occurs at a significantly higher frequency (or lower wavenumber).

At $x = 4$ cm (Figure III-13b), the lower bound of the frequency band in which the magnitude of spectral components of the forced flow is larger (i.e., $\Delta S > 0$) is at about 100 Hz, while there is less energy at lower frequencies. However, the magnitude of the positive part of ΔS is smaller than at corresponding frequencies at $x = 1$ cm indicating that the magnitude of ΔS decreases with downstream distance. Finally, at $x = 10$ cm (Figure

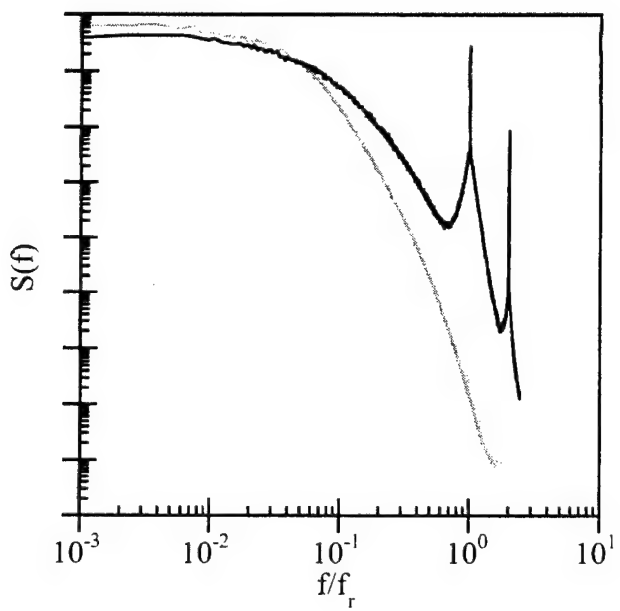


Figure III-12

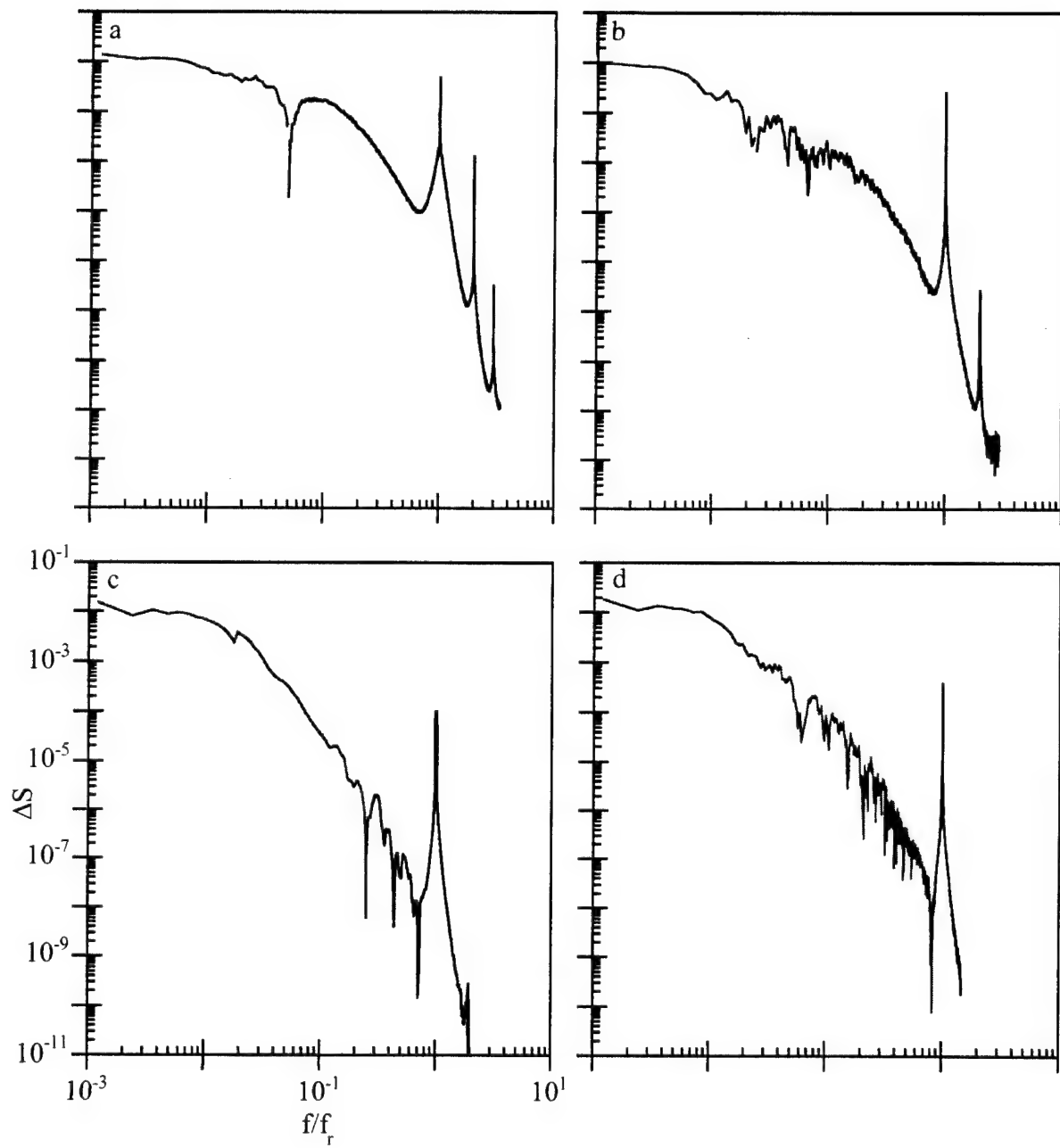


Figure III-13

III-13d), $\Delta S < 0$ (i.e., there is a decrease in spectral power at all frequencies of the forced flow) except for a narrow band around the forcing frequency. Since, as a result of the forcing, there is consistently less energy at low frequencies and more energy at high frequencies at all streamwise stations, the streamwise variation of the frequency at which ΔS changes its sign, $v_{\text{crossover}}$, is plotted in Figure III-14. The crossover frequency slowly decreases for $2 \text{ cm} \leq x \leq 6 \text{ cm}$. At this point, $v_{\text{crossover}}$ rises sharply, signifying the rapid transfer of energy from the large to the small scales.

By integrating separately the power in the frequency bands $v \geq v_{\text{crossover}}$ and $v \leq v_{\text{crossover}}$, the turbulent kinetic energy that is added to or dissipated from the flow as a result of the excitation is determined at each streamwise station and is shown in Figure III-15. At upstream locations, the total amount of energy added to the flow within the high frequency band is larger than the energy dissipated from within the low frequency band. As shown above, the spectral peak introduced by the high-frequency forcing is attenuated by an order of magnitude between $x = 5$ and 10 cm . This is reflected by the decrease in the power within the high frequency band ($v \geq v_{\text{crossover}}$). Due to the cumulative effect of the dissipation, the energy in the low frequency band ($v \leq v_{\text{crossover}}$) decreases (or ΔP increases) with downstream distance. Figure III-15 shows that at $x = 10 \text{ cm}$, the total energy dissipated reaches a value of 16% of the unforced turbulent kinetic energy.

Finally, the transfer of spectral power can be studied by looking at the power in bands of frequencies corresponding to eddies of various sizes. Eddies (as opposed to waves) consist of a band of frequencies. For example, an eddy of characteristic wavenumber k may be thought of as consisting of all wavenumbers from $0.62k$ to $(1/62)k$. The next largest eddy consists of wavenumbers from $0.24k$ to $0.62k$ (centered at $0.38k$) and so on. In this experiment, the excitation frequency provides a convenient "reference eddy" having a center frequency 5092.5 Hz (frequencies of 3157 Hz to 8213 Hz). The flowfield can be broken down into successively larger eddies (each with center frequency 0.38 times the previous one) and the power in these eddies can be calculated directly from $S(v)$.

Figure III-16 shows the power in the eddies, E_i , where E_0 is the power in the first eddy (centered at 5092.5 Hz) and E_i is the power in the successively larger eddies (centered at $0.38^i \times 5092.5 \text{ Hz} = 1957 \text{ Hz}$). Shown are the eddies for the unforced flow (open symbols) and for the forced flow (full symbols). Figure III-18a shows the large, energy-containing eddies E_2 , E_3 , and E_4 . Figure 18b shows the smaller eddies E_0 and E_1 . There is 1-2 orders of magnitude more energy in E_0 in the excited flow than in the unexcited flow. This hastens the transfer of energy from E_1 to E_0 . The power in E_1 decays significantly faster in the forced flow as its energy is transferred to the smaller scales E_0 .

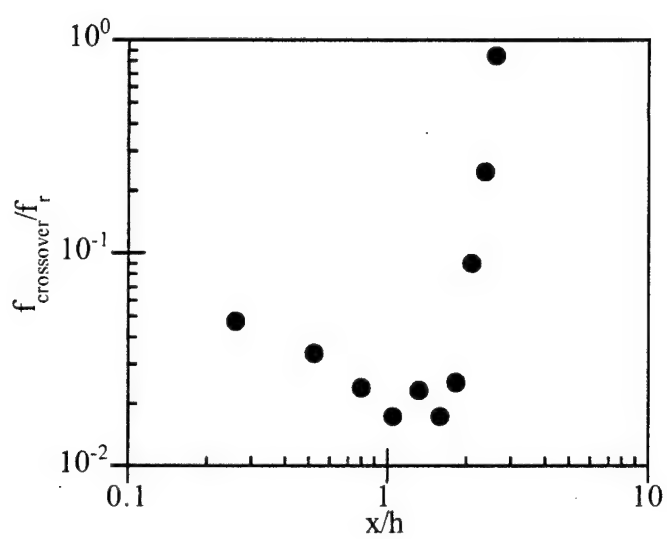


Figure III-14

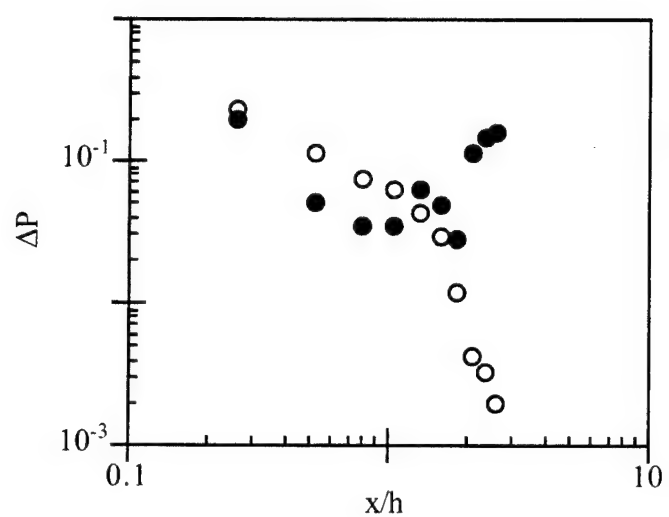


Figure III-15

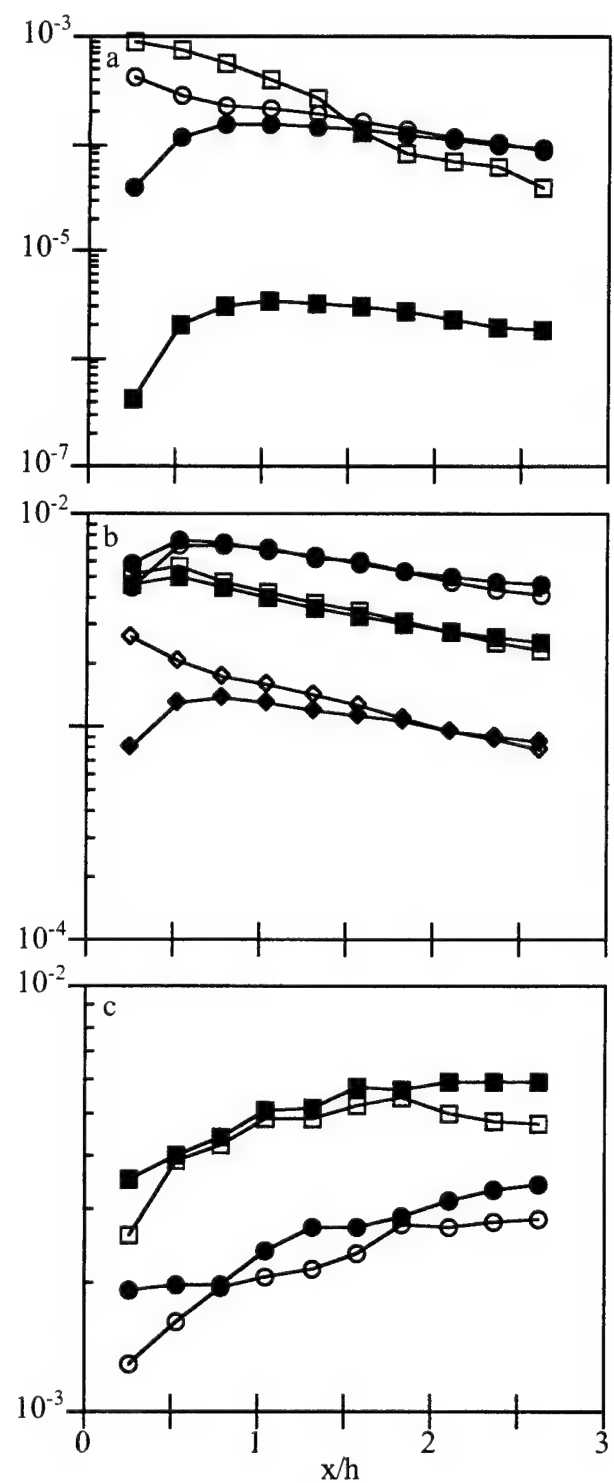


Figure III-16

Similarly, energy is transferred more rapidly from E_2 to E_1 , E_3 to E_2 , and E_4 to E_3 as a result of the forcing. Spectral energy transfer is facilitated by having high energy in the eddy to which energy is being transferred. Figure III-18a shows that the spectral power in E_4 becomes less in the forced flow than in the unforced flow at $x \approx 5$ cm. The power in E_3 becomes less at $x \approx 7$ cm, while the power in E_2 becomes less at $x \approx 8$ cm. Each eddy of a given size extracts energy from the eddies of the next larger size at a higher rate as a result of the forcing (until the energy in that eddy becomes less than in the unforced case) and in this way, forcing accelerates the cascade of energy to the dissipative region.

III.4 Conclusions

The notion of a bypass to the conventional energy cascade in turbulent shear flows by direct excitation of small scale motions is demonstrated in a shear layer segment of an air jet emanating from a square conduit (3.81 x 3.81 cm, 6.5 m/sec). Excitation near the passage frequency of the Kolmogorov scale is effected using a piezoelectric cantilevered actuator that is placed near the jet exit plane. Hot-wire measurements of cross-stream distributions of the streamwise velocity component demonstrate that even though the excitation does not alter the mean distributions of the velocity and r.m.s. velocity fluctuations within the domain of measurement, the dissipation in the forced flow increases by more than an order of magnitude relative to the unforced flow. This is not unexpected since dissipation scales with the square of the frequency and thus a small increase in velocity perturbations at high frequencies can lead to significant enhancement of the dissipation and consequently, a large decrease in the turbulent kinetic energy within the forced segment of the jet shear layer. It appears that other segments of the jet shear layer are not significantly affected by the forcing. Although the forcing frequency is well above the band of frequencies that are normally amplified by large-scale instabilities of the flow, its spectral peak is several orders of magnitude above adjacent spectral components even at the downstream end of the measurement domain, approximately 160 excitation wavelengths downstream of the actuator.

An important consequence of direct small-scale excitation is that the addition of energy at the smallest scales apparently alters the dynamics of energy cascade across a broad range of wavenumbers. The present measurements show that the excitation leads to enhanced transfer of energy from the large scales to the small scales such that in the forced flow there is more power in spectral components above a given cutoff frequency and less power in spectral component below this frequency. The reduction in the magnitude of spectral components at low frequencies suggests that the forcing induces coupling (or long-range interactions) between small and large scales within the flow and thus leads to acceleration of the conventional energy cascade and to diminution in energy associated with the large scales.

IV. VORTICITY MEASUREMENTS IN A SWIRLING JET USING ULTRASOUND SCATTERING

IV.1. Technical Background

The propagation of sound waves through turbulent flow fields results in phase and amplitude distortions of the wave fronts and wave scattering (e.g., Monin and Yaglom, 1980). In the atmosphere the distortion and scattering of sound waves is primarily effected by variations in the speed of sound due to turbulent temperature and velocity fluctuations and can be analyzed as for electromagnetic waves but with proper modification of the medium refractive index. Lighthill (1953) and Kraichnan (1953) obtained a relation between the scattering cross-section $d\Sigma$ in any direction \hat{r} of a volume V that contains the turbulence (i.e., the energy flux scattered by the volume V into a solid angle element $d\Omega$ around \hat{r} normalized by the energy flux density of the incident wave) and the correlation function of the refractive index that depends on correlation of velocity fluctuations. Predictions for the scattering cross section were given for statistically homogeneous, stationary, and isotropic turbulence, when the scattering wave numbers are within the inertial subrange.

Previous investigators have been primarily concerned with the calculation of the acoustic scattering cross-section of a turbulent flow from measurements of the velocity field. Since the scattered waves contain information regarding the scattering turbulent medium, they are useful for remote probing of the statistical characteristics of that medium. The more difficult inverse problem which is to obtain the velocity field of an unknown flow (laminar or turbulent) from measurements of scattered sound has been noted in the literature but until recently has not received much attention. Engler et. al.(1989) addressed this issue by comparing flow models with measurements of the changes in the travel time of ultrasonic waves through leading edge vortices of a delta wing, tip vortices of various oscillating wings, and the vortex field of the rotor of a wind turbine. Their measurements agree with the flow models that are based on Hamel-Oseen vortices using the vortex location, its core radius, and circulation as parameters to fit the travel time data, thus providing information on those particular flow configurations.

The scattering of ultrasound by two- and three-dimensional vortex filaments and by temperature concentration was recently studied by Lund and his co-workers (1989-1990) The analysis is within the framework of classical field theory and is based on the analogy between the interactions of electromagnetic radiation with charged particles and of sound with vortex filaments. This work has shown that when a plane acoustic wave of angular frequency ν_0 propagates through a rotational flow field (laminar or turbulent) having

characteristic time scales that are large compared to v_0^{-1} , there is a linear relationship between the Fourier component at a frequency ν of the scattered acoustic pressure in a given direction \hat{r} and the Fourier transform, in space and time, of the vorticity component that is normal to the plane defined by the wave vectors of the incident and scattered acoustic waves at frequency $\nu - v_0$. The three wave number components of the Fourier transform of the vorticity vector are determined by the frequencies and wave vectors of the incident and scattered acoustic waves so that by varying the frequency of the incident wave and \hat{r} , all three components of the wave vector of the measured Fourier component can be resolved. This means that in principle the amplitude of the Fourier transforms, in space and time, of all three components of the vorticity field can be measured non-intrusively thus suggesting a powerful means for studying vorticity scales and energy cascades between them in various shear flows.

While there is no question that there are a number of viable techniques for measurements of vorticity, the attractive features of the ultrasound scattering technique are that it is nonintrusive, requires no seeding and can, in principle, be extended to full field measurements. Furthermore, unlike conventional techniques, ultrasound scattering does not require intermediate measurements of velocity. Limited experimental testing of the theory developed by Lund and his co-workers was undertaken by Ciliberto and Pinton (1991). These authors measured the scattered acoustic pressure from a 16.5 kHz acoustic wave propagating through a Karman vortex street behind a circular cylinder at $Re = 52$. Their pressure spectra exhibit sharp maxima at the passage frequency of the Karman vortices and its first and third harmonics. These measurements are in agreement with the theory when a simple analytical model is used to model the Karman vortex street.

The present experiments are concerned with the scattering of ultrasound from the vortex that is formed at the exit plane and along the axis of a swirling jet. The jet swirl number can be varied continuously over a broad range by controlling the angular velocity of a four-blade paddle in the jet plenum. Because the jet nozzle is stationary, the net circulation about the jet axis is zero and the radial distribution of axial vorticity is nonuniform. The axial (streamwise) and tangential velocity distributions of the jet are simultaneously measured using hot wire anemometry.

IV.2. Theoretical Background

The scattering of sound by vorticity was considered by Lighthill (1953) and Kraichnan (1953) to be the consequence of the nonlinear interaction between longitudinal and transverse velocity modes. An intuitive picture of this effect can be obtained by considering the effect of a plane sound wave on a point vortex whose axis is normal to the

wave vector. The passage of the wave induces time-harmonic motion of fluid particles and, in particular, of fluid particles that are on vortex lines. This unsteady vorticity distribution results in far-field pressure fluctuations that can be interpreted as scattering of the incident sound wave. This fundamental mechanism can be extended to three dimensions and to vorticity distributions in finite domains.

A continuous distribution of vorticity within a finite domain may be treated as a concentration of tightly packed filaments. Lund (1989) used that approach to develop the expression for the acoustic pressure scattered by vorticity due to the local interaction with sound. In addition, there is a non-local interaction mediated by the potential velocity field generated by the vorticity. This additional interaction was studied by Lund and Rojas (1989) who concluded that its effect was to modify the angular dependence of the scattered radiation but not the dependence on vorticity. The end result is

$$p_s(\vec{r}, v) = \frac{p_0 v i \pi^2}{c^2 |\vec{r}|} \frac{\cos(\theta)}{\cos(\theta) - 1} e^{i k_0 |\vec{r}|} (\hat{k}_0 \times \hat{r}) \cdot \tilde{\omega}(\vec{q}, \Delta v) \quad (1)$$

where p_0 is the amplitude of pressure of the incident wave field, $\Delta v = v - v_0$ is the angular frequency difference between the scattered and the incident waves, and $\tilde{\omega}$ is the Fourier transform in space and time of the vorticity. The geometric factor $h(\theta) = \cos \theta / (\cos \theta - 1)$ provides the relationship between the scattered pressure due to the direct interaction of the sound wave with vorticity and the scattered pressure due to the interaction of the sound with the velocity field generated by the vorticity. Equation (1) establishes a relationship between p_s and the component of $\tilde{\omega}$ that is normal to the scattering plane (defined by \hat{k}_0 and \hat{r}). This equation is valid if the Mach number of the flow in question is low, the particle velocity induced by the sound wave is small in comparison with the characteristic velocity of the flow, and the sound frequency is high in comparison with the inverse of the characteristic time scales of the flow.

Finally, we note for reference below that in the swirling jet the distribution of the mean axial vorticity in cross-stream planes (i.e., normal to the jet axis) is axisymmetric, and the scattered pressure in the radial direction at a given streamwise position is determined from Eqn. (1):

$$\frac{p_s(r, v)}{p_0} = \frac{v \pi \sin(\theta) h(\theta)}{2 c^2 r} \int_0^\infty \omega(r) r dr J_0(qr) \quad (2)$$

and can be computed from a known vorticity distribution.

IV.3. The Swirling Jet

The swirling jet facility and the coordinate system are shown schematically in Figure IV-1. The jet issues from a round nozzle having an exit diameter $D = 2.54$ cm and a contraction ratio of 36:1. The swirling generator is a four-blade paddle that is placed in a 15.24 cm cylindrical tube upstream of the nozzle and is rotating about the x-axis. The distance between the downstream edge of the blades and the jet nozzle is adjustable but is set at 60 cm in the present experiments. The paddle shaft extends through the rear wall of the jet plenum and is connected to a DC motor equipped with a speed controller. The jet is driven by four radial blowers placed symmetrically around the perimeter of the plenum. Turbulence management is achieved by air filters, honeycomb materials, and screens that are placed in the plenum.

Previous investigations of swirling jets have employed a variety of swirl generators with varying degrees of effectiveness as commonly measured by the dimensionless swirl number S_w

$$S_w = \frac{2 \int_0^\infty U V r^2 dr}{D \int_0^\infty (U^2 - V^2/2) r dr} \quad (3)$$

where U and V are the mean axial and azimuthal velocity components. Regardless of the specific features of a given swirl generator, the circulation of the streamwise vorticity in the exit plane of the jet is clearly dependent on the angular velocity at the jet boundary. For a stationary boundary, the circulation at the exit plane of the jet must be identically zero owing to the no slip boundary condition. Thus, the production of axial vorticity by a given swirl generator (e.g., vanes or tangential blowing) is accompanied by the production of axial vorticity of *opposite sign* in the boundary layer of the jet nozzle. Streamwise vorticity with finite circulation can be generated only when the jet boundary is rotating.

A rotating pipe swirl generator was employed by Rose (1962) in an air jet ($Re = 1.5 \times 10^4$). Although swirl induced by a rotating tube can result in solid body rotation of the jet core, the uniformity of the axial vorticity depends critically on the length of the tube. In the experiments of Rose, the ensuing jet had relatively low swirl numbers (the maximum swirl number is estimated to be 0.21) and nonuniform streamwise vorticity distributions near the exit plane. Chigier and Chervinsky (1967) used four tangential slots in an air jet ($Re = 3 \times 10^5$) and measured swirl numbers as high as 0.64 at $x/D = 4.1$ with nearly-uniform solid body rotation within the inner region of the jet core. For $S_w > 0.4$, profiles of the streamwise velocity develop a pronounced local minimum near the jet centerline which is a precursor for the development of reversed flow and the formation of a

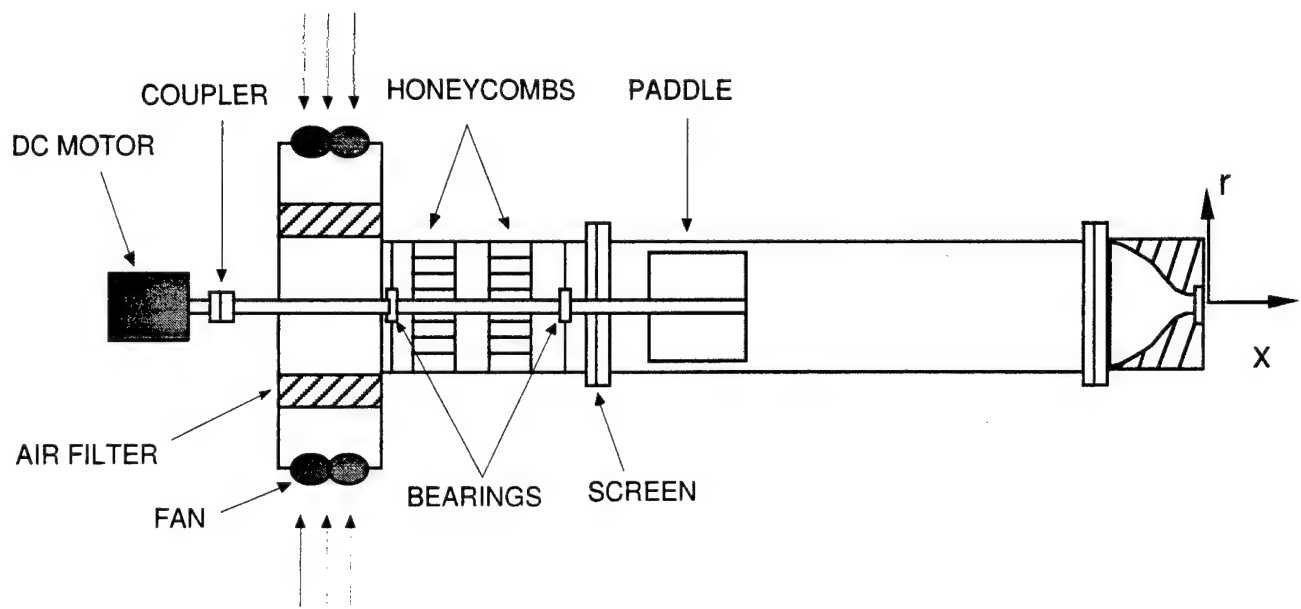


Figure IV-1

recirculation region. Tangential blowing does not allow for independent variations of the swirl number and the (mean) axial velocity and, furthermore, it does not easily lend itself to both clockwise (CW) and counterclockwise (CCW) swirl.

The present swirl generator was designed to overcome some of the disadvantages of previous designs. Although in common with these designs it produces no net circulation of the axial vorticity, this generator allows for continuous and repeatable variation of jet swirl number and for clockwise or counterclockwise reversal of the swirl. In the experiments reported here, the swirl number was kept below $Sw = 0.4$ in order to avoid the appearance of a local minimum of the axial velocity near the jet centerline. Because the rotation of the paddle increases the pressure drop through the cylindrical plenum, the power input to the jet blowers was increased with swirl number so that the jet volume flow rate (computed from radial profiles of the streamwise velocity component measured at $x/D = 0.25$) was equal to the volume flow rate in the absence of swirl at $Re = 10^4$.

Profiles of the mean streamwise and tangential velocity components ($U(r, x)$ and $V(r, x)$, respectively) were measured at a number of streamwise stations using hot-wire anemometry with an x-wire sensor. Radial distributions of the streamwise and azimuthal velocity components at $x/D = 0.25, 1, 2$ and 3 are shown on Figures IV-2 and IV-3 ($Sw = 0.24$). These data are normalized by the jet exit velocity in the absence of swirl $U_0 = 6.1$ m/sec. As a result of the swirl, there is a noticeable increase in the magnitude of the streamwise velocity near the jet centerline, and in the radial spreading of the jet shear layer. Similar changes in profiles of the streamwise velocity in swirling jets were also reported by Rose (1962) and by Sislian and Cusworth (1984).

Figure IV-3 further demonstrate that there is a limited region inside the jet core with a uniform axial vorticity distribution. Distributions of the tangential velocity component (Figure IV-3) show the existence of a radial domain around the jet centerline where $V(r, x)$ varies almost linearly with r which is indicative of solid body rotation with nominally uniform vorticity distribution. The tangential velocity attains a maximum and decays rapidly to zero. For an axisymmetric flow, the mean axial vorticity is $\omega(r) = (1/r)d[rV]/dr$ and thus radial distributions of $\omega(r)$ can be computed from the tangential velocity distributions. The radial derivative of $rV(r)$ is calculated using a standard least-squares piecewise polynomial fit to the tangential velocity data. Radial distributions of the dimensionless axial vorticity $\bar{\omega}(r) = \omega(r)/\omega_{cl}$ (where ω_{cl} is the centerline vorticity) for $x/D = 0.25, 1, 2$ and 3 are plotted in Figure IV-4. These distributions demonstrate that the jet core is comprised of distinct inner and outer radial domains marked by concentrations of axial vorticity of opposite signs. The radial spreading of these concentrations with downstream distance is connected with the evolution

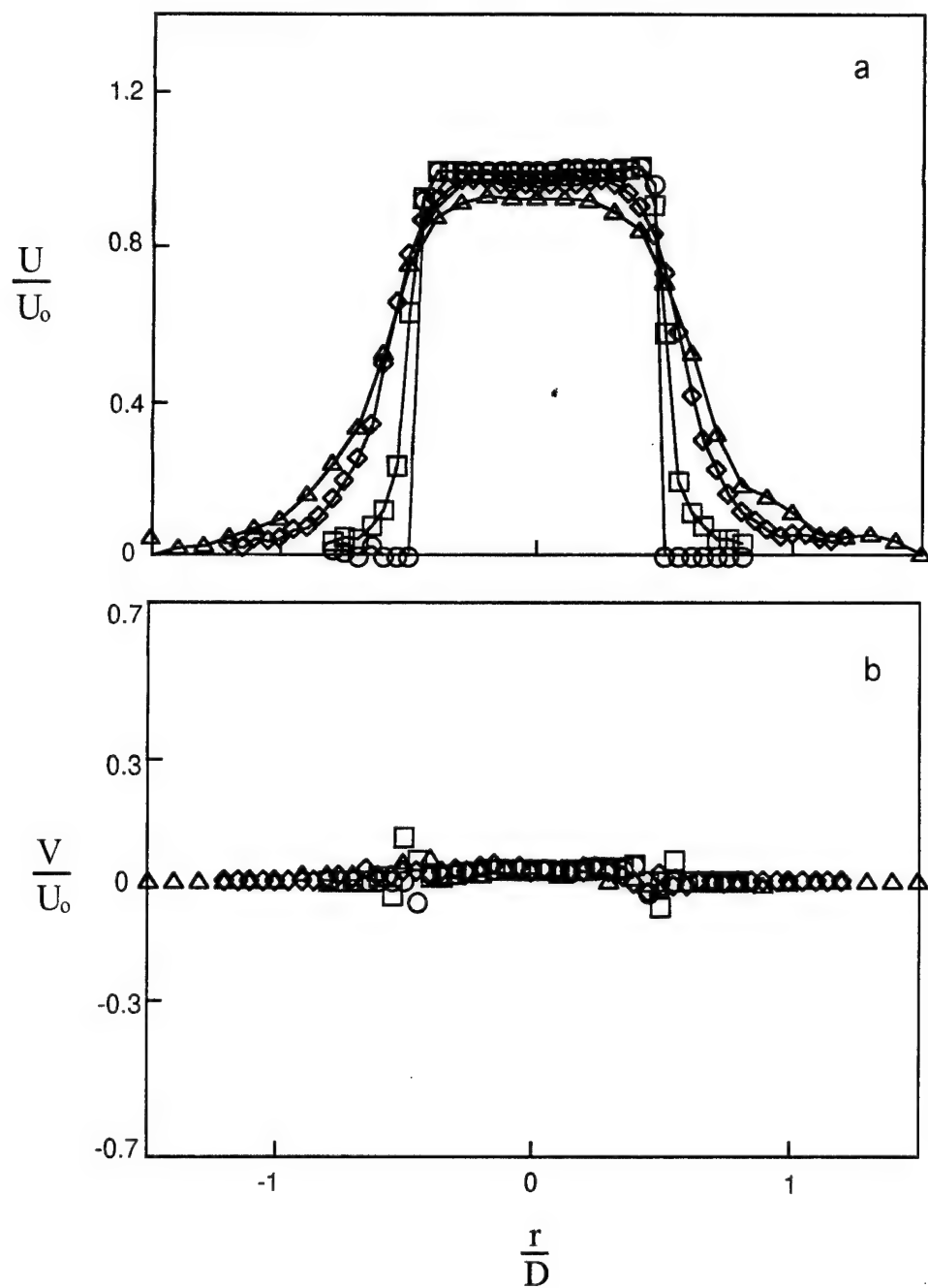


Figure IV-2

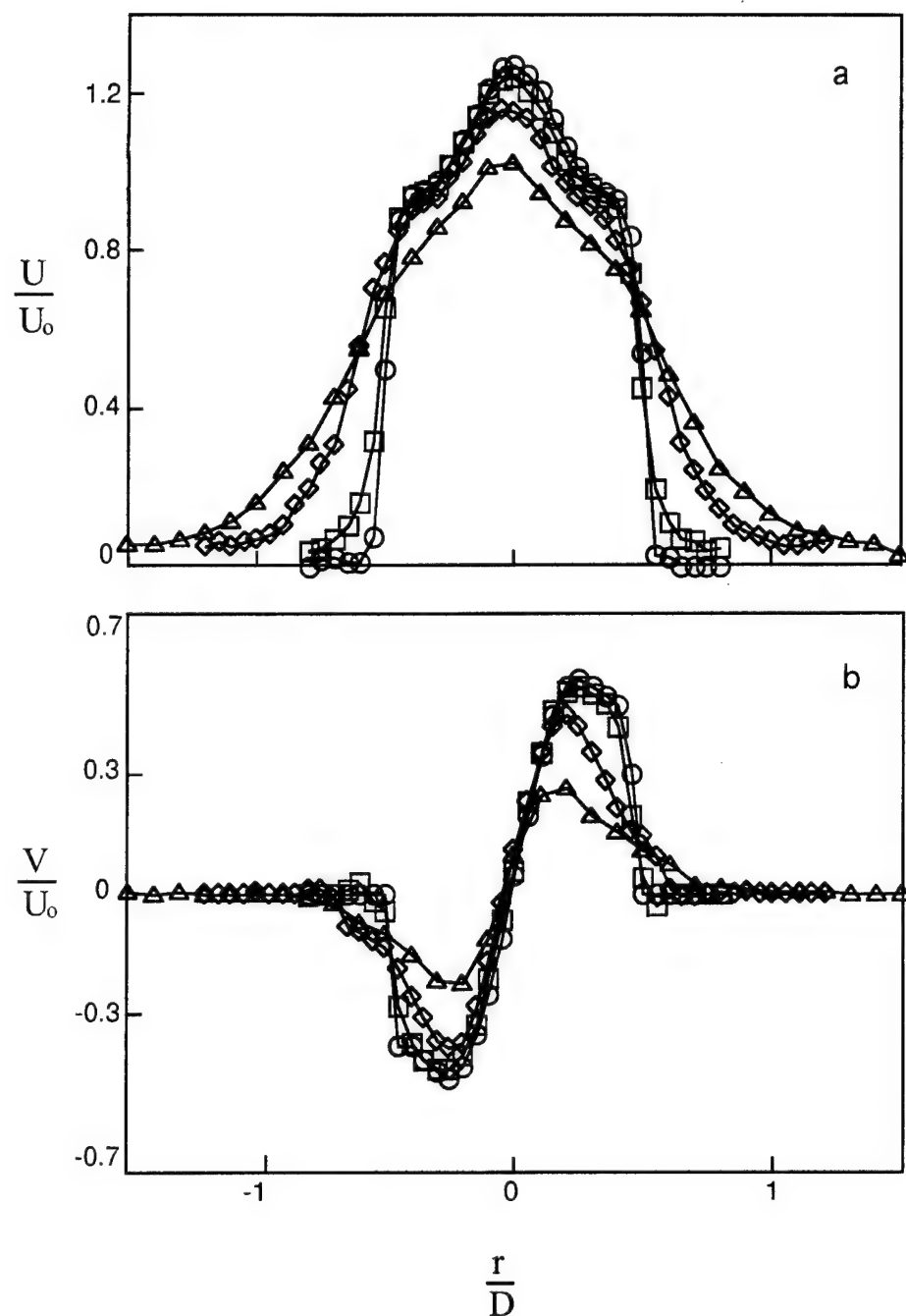


Figure IV-3

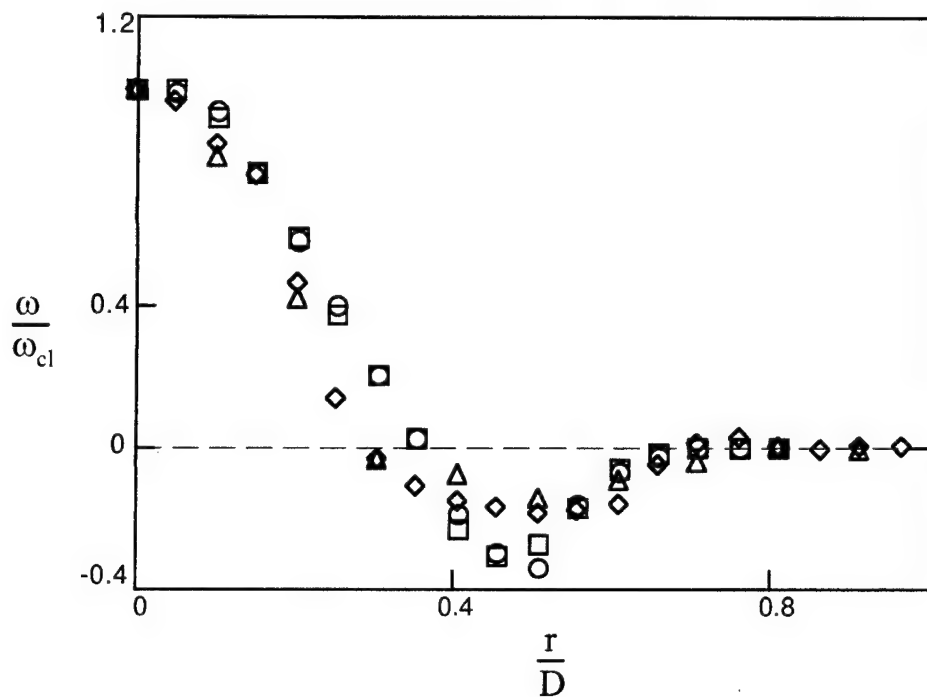


Figure IV-4

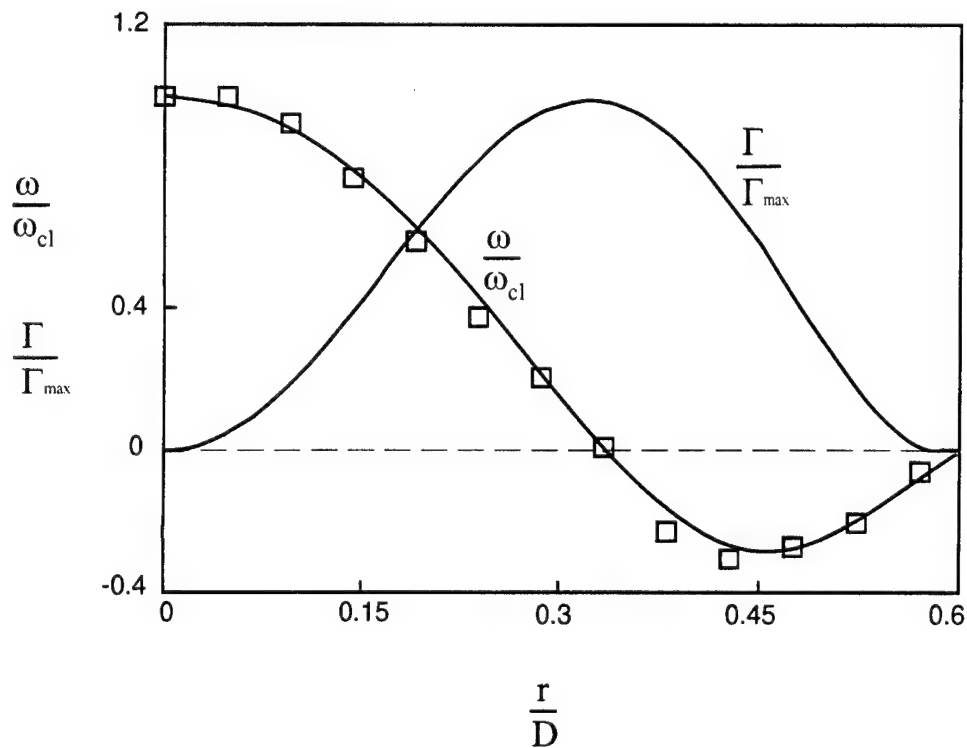


Figure IV-5

of the tangential shear layer that is induced by the swirl.

While the vorticity within the inner radial domain has the same sign as the angular velocity of the swirl generator, the vorticity in the outer domain is imposed by the stationary flow boundary. The net circulation of each of the axial vorticity distributions $\Gamma = 2\pi \int_0^\infty r\omega(r)dr$ is such that $\Gamma / \Gamma_0 < 0.01$ (Figure IV-5) where $\Gamma_0 = \pi\omega_0 r_0^2$ is the circulation at the exit plane of the jet and ω_0 is the axial vorticity on the jet centerline at $x/D = 0.25$.

IV.4. Ultrasound Scattering

A nominally plane ultrasonic wavetrain is generated normal to the jet axis by a Sell-type transmitter that utilizes an electrostatically-driven thin metal-cladded polymeric membrane. The transmitter has a square aperture measuring 16 cm on the side, its frequency bandwidth (within ± 5 dB) is 5 to 100 kHz and it is similar to the transmitter used by Baudet, Ciliberto and Pinton⁸. In the present experiments the frequency of the incident wave is $f_0 = v_0 / 2\pi = 42$ kHz. The scattered ultrasound is measured by a 6 mm-diameter B&K condenser microphone type 4135. Both the microphone and the transmitter are placed on a traversing mechanism (shown in Figure IV-6) and the transmitter is traversed azimuthally (a distance r from the centerline) at a number of streamwise stations such that its centerline intersects the jet centerlines at a right angle (the microphone output is digitized at 500 kHz). The azimuthal scattering angle between the wave vector of the incident (planar) wave field and the centerline of the microphone is θ .

As discussed in section IV.2, the measured scattered pressure field corresponds to the Fourier transform of the axial vorticity component which is normal to the plane of the incident wave vector and the centerline of the microphone (note that the Mach number of the flow is less than 10^{-2} , low enough for Eqn. (2) to apply). The normalized directional response of the microphone $\Phi(\varphi)$ (where φ is the angle between the microphone's centerline and the wave vector of an incident plane wave) is measured at 42 kHz and at 5° increments.

The power spectrum of the pressure field in the absence of swirl $E(f) = |\tilde{p}(f)|^2$ where $|\tilde{p}(f)|$ is the Fourier Transform in time of the acoustic pressure $p(t)$ is measured at $x/D = 0.25$, $r/D = 1$, and $\theta = 15^\circ$. Because the microphone is placed in the transmitted wave field, it measures the acoustic pressure of the incident wave even when $Sw = 0$ and thus $E(f)$ exhibits a spectral peak at the transmitter's frequency.

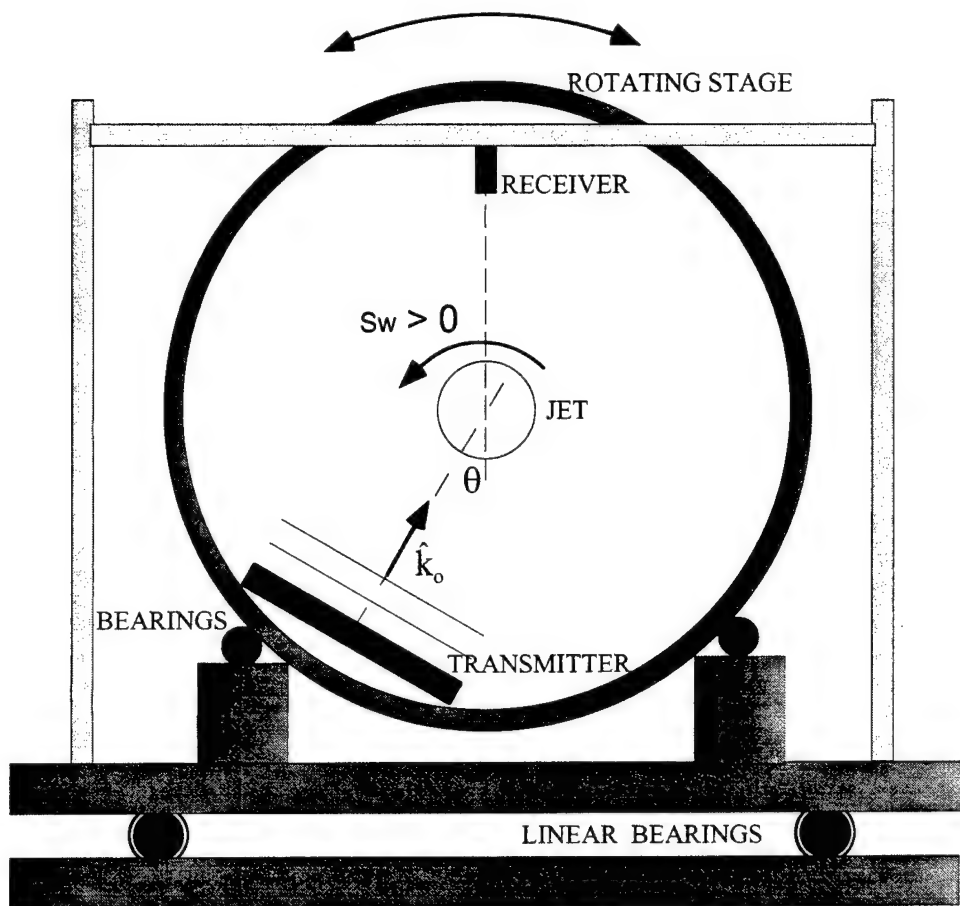


Figure IV-6

In the presence of swirl, the measured acoustic pressure is the sum of the incident and scattered acoustic pressures $\Phi \cdot \tilde{p}_i + \tilde{p}_s$ and

$$E(f) = |\Phi \cdot \tilde{p}_i + \tilde{p}_s|^2 \quad (4)$$

Thus, the normalized amplitude of the spectral peak at the transmitter's frequency η is

$$\eta = \frac{2|\tilde{p}_s| \cos(\Delta\Psi)}{|\tilde{p}_i|\Phi} \quad (5)$$

where $\Delta\Psi$ is the phase difference between the incident and scattered acoustic pressures.

When the swirl is introduced the normalized amplitude of the spectral peak increases or decreases depending on the sign of the swirl. When the swirl is CCW $\eta = 0.35$ and when the swirl is CW $\eta = -0.33$. Thus, $E(f_0)$ is sensitive to the sense of the swirl and that the increase and decrease in its magnitude are nominally the same ($\pm 2.5\%$) for CW and CCW rotation. That the power spectra of the microphone signals in the absence of swirl and when the jet is stopped (not shown) are virtually indistinguishable, indicates that in the absence of swirl the streamwise vorticity is too weak to induce measurable sound scattering. It should be noted that unlike the Karman vortices in the wake experiments of Baudet et. al. (1991) the streamwise vortex associated with the swirling jet has no net celerity normal to the jet axis even though streamwise vorticity is clearly advected axially and radially. Hence, there is no frequency shift between the transmitted and scattered waves and $\Delta\nu = 0$ in Eqn. (2).

In accord with Equation 1, Figure IV-7 ($x/D = 0.25$) show that for a given scattering angle ($\theta = \pm 15^\circ$), the magnitude of the normalized Fourier component of the measured scattered pressure $\eta(f_0)$ varies linearly with the streamwise vorticity on the jet centerline.

Furthermore, as anticipated from Equation 1, these data also demonstrate that regardless of the vorticity distribution, $\eta(f_0)/\omega_{cl}$ is independent of the amplitude (or intensity) of the incident wave field. It is noteworthy, however, that $\eta(f_0)/\omega_{cl}$ varies substantially with the scattering angle and in fact, has the same signs as θ when $\theta = \pm 15^\circ$ and opposite signs when $\theta = \pm 30^\circ$.

As discussed in section IV-2, the pressure of the scattered ultrasound can be directly computed from a known vorticity distribution. Because in the present experiments the axial vorticity of the swirling jet is independently derived from measurements of the tangential velocity component, it is possible to compare the measured and computed

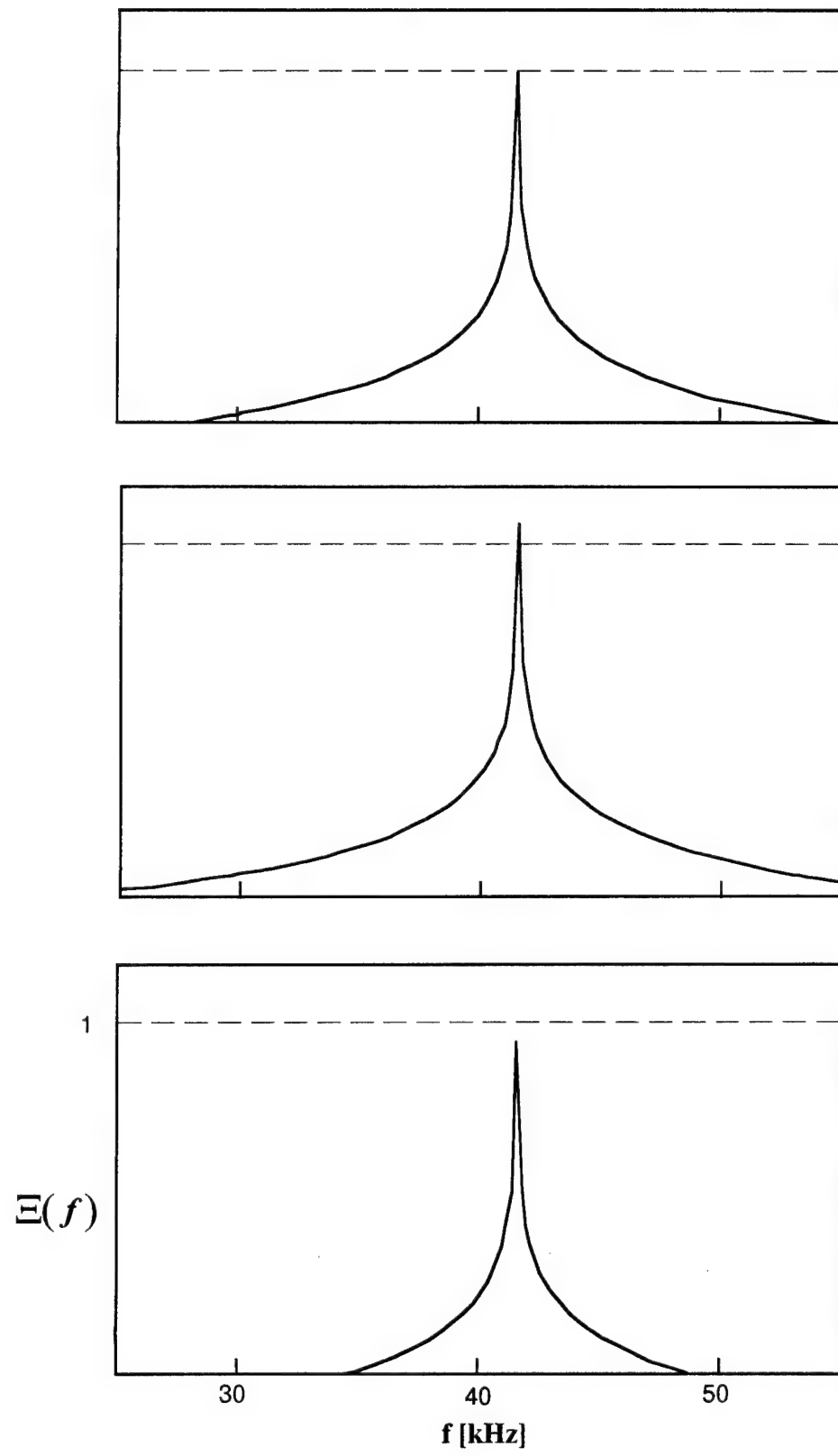


Figure IV-7

spectral components of the scattered pressure. The implication of a good agreement between measured and predicted distributions of η over a broad range of wave numbers is that the spectral components of the vorticity can be obtained *directly* from measurements of the scattered pressure. Furthermore, knowledge of the Fourier transform of a given vorticity component can, in principle, lead to the calculation of its inverse transform and thus to the vorticity distribution in physical coordinates.

The scattered pressure in a *given* direction is calculated from the measured vorticity distribution as outlined in Equation 2. Since the receiver has a finite angular response, the pressure that is actually measured may be thought of as the sum of the pressures measured by an array of small (fictitious) receivers each having a narrow angular response centered around a centerline that forms an angle ϕ relative to the centerline of the microphone. Hence, up to an overall scale factor,

$$\eta = \frac{h(\theta)\cos[\Delta\psi(\theta)]}{\Phi(\phi)} \left\{ \Phi(\phi)^* \sin(\theta) G(q_\phi) \right\} \omega_{cl} \quad (6)$$

where

$$G(q_\phi) = W_0 \cos(\phi) \int_{-A}^A e^{-iq_\phi X} \omega(X) dX \quad (7)$$

and it is assumed that the vorticity distribution is axisymmetric. In Eq. (7) $\rho^2 = X^2 + D^2 \sin^2(\phi)$ where D is the distance from the jet axis to the receiver, $q_\phi = (2v_0/c)\sin(\theta - \phi/2)$ where r_0 is the jet radius, and W_0 is the receiver width, and $A^2 = r_0 - D^2 \sin^2(\phi)$.

Note that this formulation does not specifically correct for streamwise averaging of the measured scattered ultrasound owing to the angular response of the microphone. In principle, it should be possible to use a similar convolution scheme to improve the streamwise resolution.

Measurements of the phase difference between the incident and scattered acoustic pressures ($\Delta\Psi$) were taken at $r/D = 4.5$ or $r/\lambda_0 = 15$ (where λ_0 is the wavelength of the incident wave) and the scattering angle was varied between -25° and 25° using the traversing mechanism described above. The resulting distributions of $\Delta\Psi$ (relative to $\Delta\Psi(0)$) and η (normalized with the maximum value η_M) are plotted in Figures IV-8a and IV-8b, respectively, as a function of q .

The pressure measurements were repeated at two different transmitter frequencies namely, 42 and 50 kHz (closed and open symbols, respectively). The distribution of η was also computed using the procedure outlined above where the radial distribution of

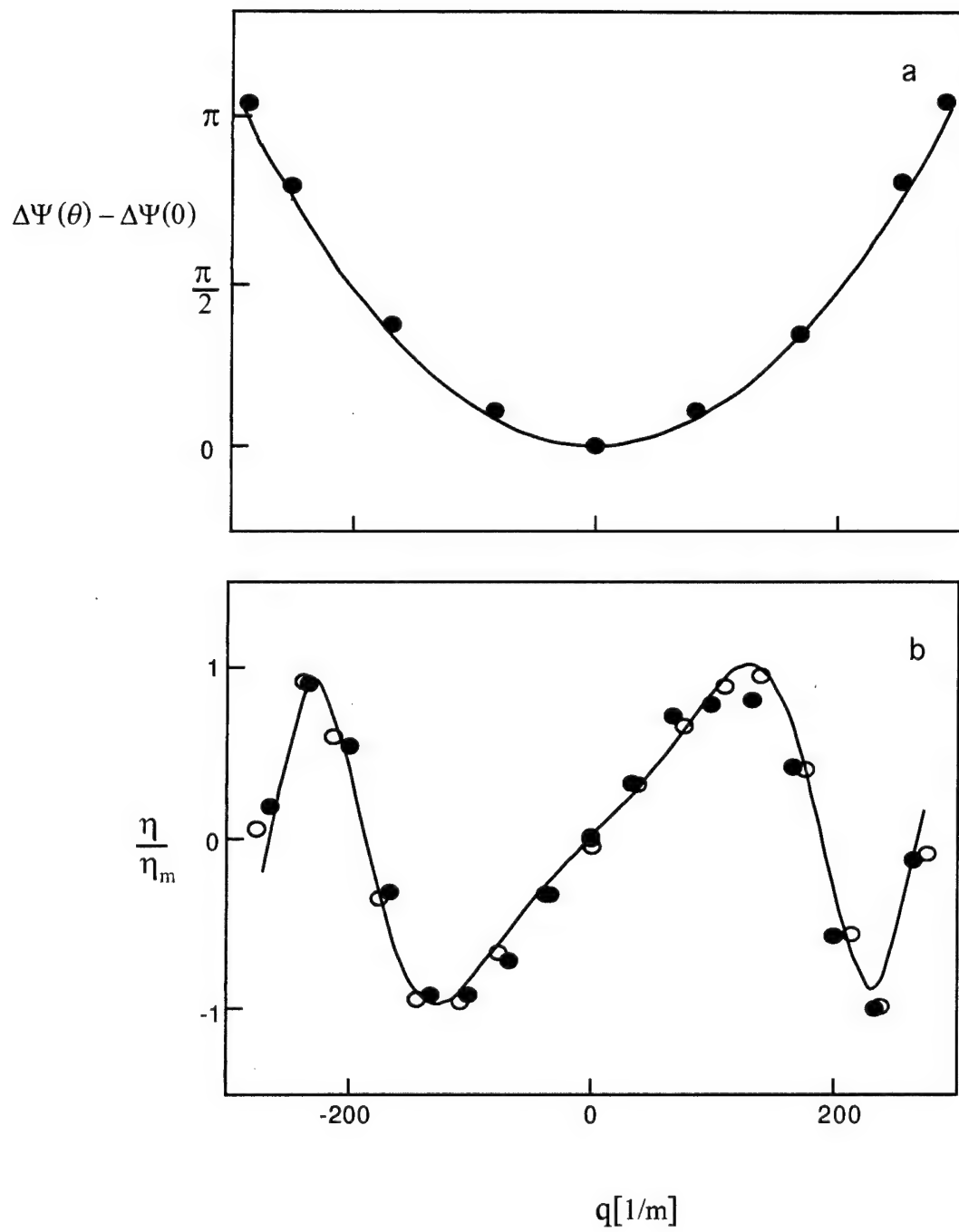


Figure IV-8

vorticity was obtained from the piecewise, least-square polynomial fit to the measured normalized axial vorticity at $x/D = 1$ and is plotted using a solid line.

As is evident in Figure IV-8b, *the agreement between the computed and measured distributions of η is remarkable* even though the computed distribution does not fully account for streamwise averaging. The remarkable agreement between the measured and computed distributions of η also suggests that the measurements are taken far enough from the jet centerline to justify the far-field approximation that is implicit in the analysis. This was further demonstrated by repeating the measurements and the calculations of η at $r/D = 6.5$. Despite the diminution in the levels of the scattered ultrasound (particularly at large scattering angles) the agreement between the measured and computed distributions of η is excellent. That η does not vary substantially with radial distance from the jet centerline implies that the measurements are indeed taken in the far field and that the receiver captures the entire cross section of the jet.

IV.5. Conclusions

The present experiments are concerned with the interrogation of a vorticity field using ultrasound scattering. More specifically, with the scattering of a plane ultrasonic wave field by an axial vorticity distribution within the core of a swirling jet. In the present experiments, the jet Reynolds number is nominally 10^4 and its swirl number is kept below 0.4 to avoid vortex breakdown and the formation of a reversed flow region. Radial distributions of the streamwise and tangential velocity components are measured at a number of streamwise stations using two-component hot wire anemometry. Corresponding distributions of the streamwise vorticity are computed, and it is verified that the net circulation about the jet axis in the absence of boundary rotation is zero while the swirl number is finite and increases linearly with the magnitude of the centerline vorticity. Ultrasound scattering is measured using a stationary, broad-band microphone and the scattering angle is varied by rotating a plane wave transmitter about the axis of the jet using a unique angular traversing mechanism. Measurements of the scattered ultrasound near the exit plane of the jet at a number of transmitter frequencies show that, in accord with theoretical predictions, the magnitude of the corresponding spectral peak of the normalized scattered pressure varies linearly with the axial vorticity on the jet centerline, is sensitive to the sense of the swirl, and is independent of the magnitude of the transmitted signal. The degree and sign of the sensitivity to the sense of the swirl depends strongly on the scattering angle.

The analysis of Lund and his co-workers suggests that direct, far-field measurements of the scattered pressure over a broad range of wave numbers correspond to

spectral measurements of the vorticity component that is normal to the wave numbers of the transmitted and scattered waves. That the Fourier transform of a given vorticity component can be directly obtained from measurements of the scattered pressure implies that, at least in principle, its inverse transform can also be computed. Thus, the primary goal of the present work has been to compare the measured and computed spectral components of the scattered pressure. Using the analysis of Lund and his co-workers, the scattered pressure is calculated from the measured vorticity distribution taking into account the finite angular response of the receiver, and is found to be in remarkable agreement with the measurements. This agreement appears to be independent of radial distance from the jet centerline and thus it is believed that the far-field approximation that is implicit in the analysis of Lund and his co-workers applies also to the present measurements.

While it has been shown that some Fourier components of the vorticity can be directly measured using ultrasound scattering, it is unclear whether the Fourier transform of the vorticity can, in fact, be realized with enough resolution to allow for the calculation of the inverse transform. At present, it appears that such measurements may be hampered by hardware limitations. For example, in the present experiments, the maximum achievable scattering angle is $\pm 25^\circ$, and it is limited by interference with side lobes of the transmitter. The spatial scale that is resolved at these angles and transmitter frequency of 42 kHz (based on the Heisenberg's principle for classical waves) is 2 cm. Although smaller spatial scales (or higher wave numbers) can be resolved by increasing the frequency of the incident wave or the scattering angle or both, it is noted that in order to resolve spatial scales on the order of 0.1 cm, the transmitter frequency at a scattering angle of 40° should be 500 kHz which may be too high for conventional microphones.

IV. LIST OF PERSONNEL

Faculty: Ari Glezer

Post Doctoral Fellow: John M. Wiltse

Graduate Students: Myodrag Oljaca, Barton L. Smith, Mark A. Trautman

V. LIST OF PUBLICATIONS

refereed

1. Oljaca, M., Gu, X., Glezer, A., Bafico, M., and Lund F., A. "Ultrasound Scattering by a Swirling Jet," submitted to *Physics of Fluids*.
2. James, R. D., Jacobs, J. W., and Glezer, A. "A Round Turbulent Jet Produced by an Oscillating Disk" accepted for publication in *Physics of Fluids*.

non-refereed

1. Jacobs, J.W., James, R. D., Ratliff, C. T., and Glezer, A. "Turbulent Jets Induced by Surface Actuators," AIAA Paper 93-3243.
2. Sutkus, D. J., Glezer, A., Rivir, R.B., and Hancock, R. "Manipulation of a Jet in a Crossflow Using Piezoelectric Actuators," AIAA Paper 94-0367.
3. James, R. D., Jacobs, J. W., and Glezer, A. "An Experimental Investigation of a Surface Jet produced by an Oscillating Surface Actuator," *Appl. Mech Rev.*, **47**, 1994.
4. Gogineni, S., Sutkus, D., Goss, L. P., and Glezer, A. "Investigation of the Flow Structure of a Forced Square Jet in a Cross Flow Using a Two-Color PIV," AIAA Paper 95-0790.
5. Oljaca, M., Glezer, A., Gu X., Baffico, M. and Lund F. "Vorticity Measurements in a Swirling Jet Using Ultrasound Scattering," AIAA Paper 96-0437.
6. Wiltse, J. M. and Glezer A. "Direct High-Frequency Excitation Of Turbulence In Free Shear Flows," AIAA Paper 96-0309.
7. Kibens, V., Parekh, D. E., Bingaman, D. C., Glezer, A., Mossman, M. F., and Rogers, C. B. "Innovative Jet Flow Control: Technology Transfer Process," AIAA Paper 96-0307.
8. Parekh, D. E., Kibens V., Glezer, A., Wiltse, J. M., and Smith, D. M. "Innovative Jet Flow Control: Mixing Enhancement Experiments," AIAA Paper 96-0308.

VI. INTERACTIONS AND TRANSITIONS

VI.1. Collaboration with McDonnell Douglas Aerospace (MDA) on Synthetic Jet Technology

In collaborative research program MDA and Georgia Tech are jointly developing a series of novel actuator concepts for mixing enhancement, thrust vectoring, and aerodynamic shape modification. Based on the research work supported by AFOSR at Georgia Tech, these concepts employ pulsatile zero-mass-flux synthetic jet actuators and cantilevered bimorph piezoelectric actuators. Fluidic actuators are used in the development of vectoring nozzle concepts by exploiting virtual Coanda surfaces for advanced-nozzle plume vectoring, while the piezoelectric actuators are used for mixing enhancement and noise control applications in high-speed flows.

These activities are a part of MDA Active Control Technology Development Program that is aimed at achieving efficient methods for manipulation and control of turbulent shear flows associated in external aerodynamics and propulsion applications. Systems requirements that have driven this work include noise reduction needs of the HSCT, temperature reduction needs associated with the C-17 nacelle redesign program, and, most recently, the intent to replace heavy, mechanically complex advanced fighter engine thrust vectoring devices with fluidic-control based vectoring schemes. MDA was recently awarded a task under the WL FLINT program whose objective is to address the issues of high speed plume vectoring as driven by the needs of advanced nozzle design. The approach intended is to further develop the technology described above to demonstrate the feasibility of vectoring for supersonic flows. The work will consist of a number of coordinated activities including investigations of the interaction between the primary and control jets and supersonic jet receptivity experiments, actuator development, design, fabrication and testing.

VI.2. Other transitions of Synthetic Jet Technology

Thermal management technologies based on microjet cooling to be implemented in single- and multi-chip module packages:

NSF-ERC at Georgia Tech (R. Tummala, Director)

IBM Research Center (Dr. R. Chu)

MICOM (Army Missile Command Mr. P. Black).

VII. PATENT APPLICATION

Glezer, A. *et al.*, "Synthetic Jet Actuator and Applications Thereof", US Patent Application, **pending**.

REFERENCES

Baudet, C., Ciliberto, S. & Pinton, J. F. "Spectral analysis of the von Karman flow using ultrasound scattering," *Phys. Rev. Lett.* **67**, 193 (1991).

Champagne, F.H. 1978 The fine-scale structure of the turbulent velocity field. *J. Fluid Mech.* **86**, 67-108.

Chigier, N. A. & A. Chervinsky, "Experimental investigation of swirling vortex motion in jets," *J. Appl. Mech.* **34**, 443 (1967).

Coe, D.J., Allen, M.G., Smith, B.L. & Glezer, A. 1995 Addressable micromachined jet arrays. *Technical Digest: TRANSDUCERS '95*. Stockholm, Sweden.

Coe, D.J., Allen, M.G., Trautman, M.A. & Glezer, A. 1994 Micromachined jets for manipulation of macro flows. *Technical Digest: Solid-State Sensor and Actuator Workshop*, 243-247.

Contreras, H. & Lund, F. "Ultrasound as a probe of turbulence II: Temperature inhomogeneities," *Phys. Lett. A* **149**, 127 (1990).

Davidson, B.J. & Riley, N. 1972 Jets induced by oscillatory motion. *J. Fluid Mech.* **53** part 2, 287-303.

Engler, R. H., Schmidt, D. W. & Wagner, W. J. "Nondisturbing acoustical measurements of flow fields -- new developments and applications," *J. Acoust. Soc. Am.*, **85**, 72 (1989) and references therein.

Glezer, A. & Coles, D. 1990 An experimental study of a turbulent vortex ring. *J. Fluid Mech.* **211**, 243-283.

Ho, C.-M. & Huerre, P. 1984 Perturbed free shear layers. *Ann. Rev. Fluid Mech.* **16**, 365-424.

Huang, L.S., Bryant, T.D. & Maestrello, L. 1988 The effect of acoustic forcing on trailing edge separation and near wake development of an airfoil. *AIAA paper* 88-3531-CP.

Huang, L.S., Bryant, T.D. & Maestrello, L. 1987 Separation control over an airfoil at high angles of attack by sound emanating from the surface. *AIAA paper* 87-1261.

James, R.D., Jacobs, J.W. & Glezer, A. 1994 An experimental investigation of a turbulent jet produced by an oscillating surface actuator. Submitted to *Physics of Fluids*.

Joyce, J.W. 1983 Fluidics--Basic component and applications, *Special Report* HDL-SR-83-9.

Kraichnan, R. H. "The scattering of sound in a turbulent medium," *J. Acoust. Soc. Am.*, **25**, 1096 (1953).

Lighthill, M. J. "On the energy scattered from the interaction of turbulence with sound or shock waves," *Proc. Camb. Phil. Soc.*, **49**, 531 (1953).

Lund, F. "Response of a filamentary vortex to sound," *Phys. Fluids A* **1**, 1521 (1989).

Lund, F. & Rojas, C. "Ultrasound as a probe of turbulence," *Physica D* **37**, 508 (1989).

Mednikov, E.P. & Novitskii, B.G. 1975 Experimental study of intense acoustic streaming. *Sov. Phys. Acoust.* **21**, 152-154.

Monin, A. S. & Yaglom, A. M., *Statistical Fluid Mechanics*, MIT Press, (1980).

Neuberger, D. & Wygnanski, I. 1987 The use of a vibrating ribbon to delay separation on two dimensional airfoils. *Proceedings of Air Force Academy Workshop on Unsteady Separated Flow* (Colorado Springs, CO), edited by F. J. Seiler, Research Labs. Rept. TR-88-0004, U. S. Air Force Academy, 1987.

Nyborg, W.L. 1953 Acoustic streaming due to attenuated plane waves. *J. of the Acoustical Society of America*. **25**, 68-75.

Nygaard, K. J. & Glezer, A. 1991 Evolution of streamwise vortices and generation of small-scale motion in a plane shear layer. *J. Fluid Mech.* **231**, 257-301.

Ostrovskii, L.A. & Papilova, I.A. 1974 Nonlinear acoustic streaming. *Sov. Phys. Acoust.* **20**, 45-49.

Rose, W. G. "A swirling round turbulent jet," *J. Appl. Mech.* **29**, 615 (1962).

Raman, G. & Cornelius, D. 1995 Jet mixing control using excitation from miniature oscillating jets. *AIAA Journal*. **33**, 365-368.

Riley, N. & Wibrow, M.F. 1995 The flow induced by the torsional oscillations of an elliptic cylinder. *J. Fluid Mech.* **290**, 279-298.

Roberts, F.A. 1985 Effects of a periodic disturbance on structure and mixing in turbulent shear layers and wakes. Ph.D. Thesis, California Institute of Technology.

Roberts, F.A. & Roshko, A. 1985 Effects of periodic forcing on mixing in turbulent shear layers and wakes. *AIAA Shear Flow Control Conf.* March 12-14, Boulder, Colorado.

Roshko, A. 1993 Perspectives on bluff body aerodynamics. *J. of Wind Engineering and Industrial Aerodynamics*. **49**, 79-100.

Seifert, A., Bachar, T., Koss, D., Shephelovich, M. & Wygnanski, I. 1993 Oscillatory blowing: a tool to delay boundary-layer separation. *AIAA Journal*. **31**, 2052-2060.

Sheen S.H., Lawrence, W.P. & Raptis, A.C. 1989 Cavitation-controlled ultrasonic agitator. *Proceedings of the IEEE 1989 Ultrasonics Symposium*. **1**, 653-656.

Sigurdson, L.W. & Roshko, A. 1985 Controlled unsteady excitation of a reattaching flow. *AIAA paper* 85- 00552.

Sislian, J. P. & Cusworth, R. A. "Laser Doppler velocimetry measurements of mean velocity and turbulent stress tensor components in a free isothermal swirling jet," *UTIAS Report*, No. 281 (1984).

Smith, B.L. & Glezer, A. 1994 Vectoring of a high aspect ratio rectangular jet using a zero net mass flux control jet. *Bul. Am. Phys. Soc.* **39**, 1894.

Stuart, J.T. 1966 Double boundary layers in oscillatory viscous flow. *J. Fluid Mech.* **24**, 673-687.

Tennekes, H. and Lumley, J.L. 1972 *A First Course in Turbulence*, MIT Press, Cambridge.

Viets, H. 1975 Flip-flop jet nozzle, *AIAA Journal*. **13**, 1375-1379.

Wehrmann, O.H. 1965 Reduction of velocity fluctuations in a Karman vortex sheet by a vibrating cylinder. *Phys. Fluids* . **8**, 760-761.

Wehrmann, O.H. 1967a The influence of vibrations on the flow field behind a cylinder. *Document D1-82-0619*. Boeing Scientific Research Laboratories.

Westerveldt, P.J. 1953 The theory of steady rotational flow generated by a sound field. *J. of the Acoustical Society of America..* **25**, 60-67.

Williams, D.R., Acharya, M., Bernhardt, J. & Yang, P. 1991 The mechanisms of flow control on a cylinder with the unsteady bleed technique. *AIAA paper* 91-0039.

Williams, D.R. & Amato, C.W. 1988 Unsteady pulsing of cylinder wakes. *AIAA paper* 88-3532-CP.

Williams, D. & Bernhardt, J. 1990 Proportional control of asymmetric forebody vortices with the unsteady bleed technique. *AIAA paper* 90-1629.

Wiltse, J.M. 1993 Control of mixing in a nonreactive shear layer, Ph.D. Dissertation, University of Arizona.

Wiltse, J. & Glezer, A. 1995 (in preparation) Control of mixing in a nonreactive plane shear layer. Part I. Open loop control.

Wiltse, J. & Glezer, A. 1995 (in preparation) Control of mixing in a nonreactive plane shear layer. Part II. Feedback control.

Wiltse, J.M. & Glezer, A. 1993 Manipulation of free shear flows using piezoelectric actuators. *J. Fluid Mech.* **249**, 261-285.

Wiltse, J.M. & Glezer, A. 1994 Small -scale mixing in free shear flows. *Bul. Am. Phys. Soc.* **39**, 1967.

Yeung, P.K., Brasseur, J.G. & Wang, Q. 1995 Dynamics of direct large-small scale couplings in coherently forced turbulence: concurrent physical- and Fourier-space views. *J. Fluid Mech..* **283**, 43-95.